

Banner appropriate to article type will appear here in typeset article

Evolution of internal cnoidal waves with local defects in a two-layer fluid with rotation

Korsarun Nirunwiroj¹, Dmitri Tseluiko¹, Karima Khusnutdinova^{1†}

¹Department of Mathematical Sciences, Loughborough University, Loughborough LE11 3TU, UK

(Received xx; revised xx; accepted xx)

Internal waves in a two-layer fluid with rotation are considered within the framework of Helfrich's f-plane extension of the Miyata–Choi–Camassa (MCC) model. Within the scope of this model, we develop an asymptotic procedure which allows us to obtain a description of a large class of uni-directional waves leading to the Ostrovsky equation and allowing for the presence of shear inertial oscillations and barotropic transport. Importantly, unlike the conventional derivations leading to the Ostrovsky equation, the constructed solutions do not impose the zero-mean constraint on the initial conditions for any variable in the problem formulation. Using the constructed solutions, we model the evolution of quasi-periodic initial conditions close to the cnoidal wave solutions of the Korteweg–de Vries (KdV) equation but having a local amplitude and/or periodicity defect, and show that such initial conditions can lead to the emergence of bursts of large internal waves and shear currents. As a by-product of our study, we show that cnoidal waves with periodicity defects discussed in this work are weak solutions of the KdV equation and, being smoothed in numerical simulations, they behave as long-lived approximate travelling waves of the KdV equation, with the associated bursts being solely due to the effect of rotation.

Key words: Internal waves, Ostrovsky equation, weak solutions of the KdV equation, rogue waves

1. Introduction

The Korteweg–de Vries- and Ostrovsky-type family of models plays an important role in understanding the behaviour of long nonlinear internal waves commonly observed in coastal seas, narrow straits and river-sea interaction areas (see Grimshaw et al. 1998; Helfrich and Melville 2006; Bona et al. 2008; Ostrovsky et al. 2015; Khusnutdinova and Zhang 2016; Ostrovsky et al. 2024, and references therein). The Ostrovsky equation (Ostrovsky 1978)

$$(A_t + \nu AA_\xi + \lambda A_{\xi\xi\xi})_\xi = \gamma A \quad (1.1)$$

is a rotationally modified extension of the integrable Korteweg-de Vries (KdV) equation (Boussinesq 1871; Korteweg and de Vries 1895; Gardner et al. 1967), accounting for the

† Email address for correspondence: K.Khusnutdinova@lboro.ac.uk

leading order balance of weak nonlinear, dispersive and rotational effects. In the general setting of a density stratified fluid described by the Euler equations with boundary conditions appropriate for oceanic applications, equation (1.1) is written for the amplitude $A(\xi, T)$ of a single plane internal mode $\phi(z)$ in a reference frame moving with the linear long wave speed c_0 . In physical variables where the bottom is at $z = -h$ and unperturbed surface is at $z = 0$, the modal equations have the form

$$(\rho_0 W^2 \phi_z)_z + \rho_0 N^2 \phi = 0, \quad (1.2)$$

$$\phi = 0 \quad \text{at} \quad z = -h, \quad \text{and} \quad W^2 \phi_z = g\phi \quad \text{at} \quad z = 0. \quad (1.3)$$

Here $\rho_0(z)$ is the stable background density profile, $N^2 = -g\rho_{0z}/\rho_0$, $W = c_0 - u_0$, where $u_0(z)$ is the background shear flow supported by a body force, and it is assumed that there are no critical levels, that is $W \neq 0$ for any z in the flow domain. The nonlinear, dispersive and rotational coefficients ν , λ and γ , respectively, are given by

$$I\nu = 3 \int_{-h}^0 \rho_0 W^2 \phi_z^3 dz, \quad I\lambda = \int_{-h}^0 \rho_0 W^2 \phi^2 dz, \quad I\gamma = f^2 \int_{-h}^0 \rho_0 \Phi \phi_z dz, \quad (1.4)$$

where

$$I = 2 \int_{-h}^0 \rho_0 W \phi_z^2 dz, \quad \rho_0 W \Phi = \rho_0 W \phi_z - (\rho_0 u_0)_z \phi, \quad (1.5)$$

and f is the Coriolis parameter (a reduction of the bi-modal system derived in Alias et al. 2013). Note that when there is no shear flow, that is $u_0(z) \equiv 0$, then $\Phi \equiv \phi_z$ and $\gamma = f^2/2c$; in this case $\lambda\gamma > 0$, but sufficiently strong shear near a pycnocline may lead to a situation where $\beta\gamma < 0$ (Alias et al. 2014).

The Ostrovsky equation became a paradigm forming model for studying the effects of rotation on the evolution of internal waves with the natural initial conditions in the form of KdV solitons (see Grimshaw et al. 2013; Stepanyants 2020; Ostrovsky et al. 2024 and references therein) and cnoidal waves, with an emphasis on modulational instability (see Whitfield and Johnson (2017) and references therein), as well as the related qualitative analysis of the long-time asymptotics of strongly-interacting internal modes described by solutions of coupled Ostrovsky equations (Alias et al. 2014). One of the aims of our current study is to extend the modelling to situations when the initial conditions are close to a cnoidal wave (approximately a chain of KdV solitons), but they are not perfectly periodic, and rather have some defects within the computational domain (hence, they can be viewed as being quasi-periodic). The motivation for that stems from the observational data of the type shown in Figure 1, where we can see formation of a wavetrain of internal solitary waves close to an imperfect cnoidal wave. Indeed, given that the waves generally propagate in variable environment, quasi-periodic initial conditions seem to be a more natural choice than a single (pure or only slowly modulated) cnoidal wave. Recently, there appeared renewed interest in the possibility of generating rogue waves and breathers by various localised perturbations of cnoidal waves both in integrable and non-integrable settings (see Kuznetsov & Mikhailov 1975; Onorato et al. 2013; Chabchoub et al. 2013; Kedziora et al. 2014; Maiden and Hoefel 2016; Chabchoub et al. 2021; He et al. 2022; Bertola et al. 2023; Grava et al. 2023; Hoefel et al. 2023; Mao et al. 2023; Chandramuli et al. 2024, and references therein), among other possible mechanisms (e.g. Kharif et al. 2009; Zakharov 2009; Pelinovsky and Slunyaev 2016; Bokaeyan et al. 2019; Choi et al. 2022; Slunyaev and Shrira 2023; Agafontsev et al. 2024; Congy et al. 2024; Flamarion et al. 2024; Slunyaev 2024, and references therein). Our study extends the former line of research by adding the effect of rotation.

Unlike the KdV equation, the Ostrovsky equation has a constraint on the mean value of

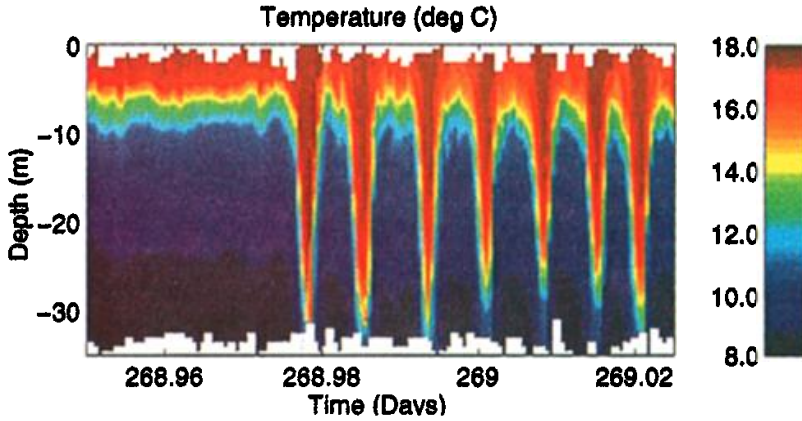


Figure 1: The first 1.7 hours of the colour contour time series of temperature profiles off Northern Oregon from the surface to 35m depth. The figure is adapted from Stanton and Ostrovsky (1998).

its regular solutions. For example, for periodic solutions on the interval $[-L, L]$, any regular solution should have zero mean:

$$\int_{-L}^L A \, d\xi = 0. \quad (1.6)$$

Additional constraints appear when solutions are considered in the class of functions vanishing at infinity (Benilov 1992). The existing derivations of the Ostrovsky equation from the Euler equations do not allow one to consider the arbitrary initial conditions for the field variables of the parent system, but only those which agree with this constraint. This restriction on the choice of initial conditions of the Cauchy problem for the parent system became known as the “zero-mean contradiction”. Hence, another aim of our study is to generalise the construction of weakly-nonlinear solutions leading to the Ostrovsky equation in such a way that the zero-mean contradiction is avoided. Indeed, this has been previously done within the scope of the derivation of Ostrovsky-type models in the simpler settings of the Boussinesq-Klein-Gordon and coupled Boussinesq equations (Khusnutdinova et al. 2014; Khusnutdinova and Tranter 2019, 2022). In contrast to the previous work, in the fluids context the mean-field equations appear to be coupled to equations for deviations from the mean values, presenting a significant new challenge, which is addressed in our present paper.

Hence, the aim of our study is twofold, and the rest of the paper is organised as follows. In Section 2 we introduce Helfrich’s rotation-modified two-layer Miyata–Choi–Camassa (MCC-f) model (Helfrich 2007) and obtain its simpler weakly-nonlinear reduction which is used to develop the subsequent (weakly-nonlinear) derivations of the reduced model (for the original MCC model see Miyata 1988; Choi and Camassa 1996, 1999, but also Maltseva 1989, where the same system has been derived and studied). While this setting is simpler than the full Euler equations, our derivations reveal that it retains the key complexity: the mean-field equations are coupled with the equations for the deviations. Therefore, this model provides an appropriate framework for our developments. Next, in Section 3 we refine the derivation of the uni-directional model by considering the simultaneous evolution of mean fields and their deviations. This approach introduces the fast characteristic variable $\xi = x - c_0 t$ and two slow-time variables $\tau = \sqrt{\alpha} t$ and $T = \alpha t$, rather than just one, where α is the small amplitude parameter (we assume the maximum balance conditions for the weak nonlinearity, dispersion and rotation). We find a way to by-pass the zero-mean contradiction by developing simultaneous asymptotic expansions of both the mean-field variables and deviations. This

allows us to construct a more general class of solutions allowing the initial conditions for all fluid variables to have arbitrary (and generally time-dependent) mean values, while the emerging Ostrovsky equations have zero mean by construction. In Section 4 we use the constructed weakly-nonlinear solution combined with numerical modelling using the Ostrovsky equation in order to investigate the effect of rotation on the evolution of cnoidal waves of the KdV equation close to their solitonic limit and having local amplitude and/or periodicity defects. We begin the section by considering the effect of rotation on simple soliton and cnoidal wave solutions, as well as dark and bright breathers of the KdV equation and contraction and expansion periodicity defects in order to set up the phenomenological framework for the discussion of our main numerical results. The contraction / expansion defects are introduced by extracting a small symmetric piece around the trough and gluing the remaining parts together / by cutting the cnoidal wave at the trough and symmetrically inserting a piece of straight line, respectively, see the first two rows of Figure 17 in Appendix A. In all cases we take a sufficiently large computational domain and impose the periodic boundary conditions to model the resulting quasi-periodic solutions. We show that, combined with the effect of rotation, initial conditions in the form of cnoidal waves with local defects can lead to bursts of large amplitude internal waves and shear currents. For the generic local defects introduced by adding a localised perturbation, this can be attributed to the formation of a pair of bright and dark breathers and contraction and expansion periodicity defects, with the subsequent effect of rotation. For the pure expansion and contraction defects the bursts do not take place without rotation. In fact, in numerical runs the smoothed counterparts of such initial conditions evolve almost like travelling wave solutions of the KdV equation, for a very long time. We show that this happens because these functions (and some other functions constructed from the known KdV solutions by similar procedures) satisfy all (infinitely many) conservation laws of the KdV equation (see Appendix A). Moreover, a cnoidal wave with an expansion defect has a continuous first derivative, satisfying the Weirstrass-Erdmann corner condition for broken (non-smooth) extremals (e.g. Fox 1954), and it is a weak solution of the KdV equation. The bursts observed in our modelling with pure periodicity defects are then attributed solely to the effect of rotation. Moreover, we show that the effects discussed in the paper are structurally stable with respect to the natural (compatible with the period of the background cnoidal wave) variations in the size of the computational domain. We finish with a discussion in Section 5, where we also show an example where a local perturbation of a cnoidal wave of the type considered in our paper has led to the generation of a rogue wave. A pseudospectral scheme used to solve the Ostrovsky equation is discussed in Appendix B.

2. MCC-f model

We consider the f-plane extension of the MCC model for an inviscid, incompressible two-layer fluid with the rigid lid introduced by Helfrich (2007):

$$h_{it} + (h_i \bar{u}_i)_x = 0, \quad (2.1)$$

$$\bar{u}_{it} + \bar{u}_i \bar{u}_{ix} - f \bar{v}_i = -g \eta_x + \frac{1}{\rho_i} P_x + D_i, \quad \text{where} \quad (2.2)$$

$$D_i = h_i^{-1} \left\{ \frac{h_i^3}{3} [\bar{u}_{ixt} + \bar{u}_i \bar{u}_{ixx} - (\bar{u}_{ix})^2] \right\}_x, \quad (2.3)$$

$$(h_i \bar{u}_i)_t + (h_i \bar{u}_i \bar{v}_i)_x + f h_i \bar{u}_i = 0, \quad (2.4)$$

$$\bar{v}_{it} + \bar{u}_i \bar{v}_{ix} + f \bar{u}_i = 0. \quad (2.5)$$

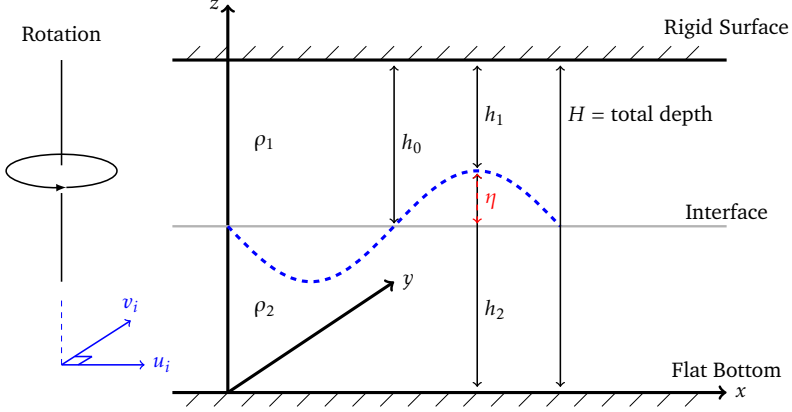


Figure 2: Schematic of a two-layer fluid with rotation in the rigid-lid approximation.

Here, h_i , ρ_i are the layer depths and densities, \bar{u}_i, \bar{v}_i denote the depth-averaged over each layer horizontal velocities in the x and y directions with $i = 1$ and 2 referring to the upper and lower layers, respectively; f is the Coriolis parameter, g is gravity, P is the pressure at the interface. The subscripts t and x denote partial derivatives. In the absence of motion $h_1 = h_0$ and $h_1 + h_2 = H$ (total depth) (see Figure 2).

In the Boussinesq approximation ($\frac{\rho_2 - \rho_1}{\rho_1} \ll 1$), the equations can be simplified by eliminating P_x . Using $\sqrt{g'H}$, H , l and $l/\sqrt{g'H}$ to non-dimensionalise (u_i, v_i) , h_i , x and t , respectively, and changing the variables to $s = \bar{u}_2 - \bar{u}_1$, $v = \bar{v}_2 - \bar{v}_1$, $h_2 = 1 - h_1$, $U = h_1 \bar{u}_1 + h_2 \bar{u}_2$ and $V = \bar{v}_1 h_1 + \bar{v}_2 h_2$ with the barotropic transport in x direction $U = F(t) \neq 0$ in general, we obtain

$$\eta_t + (c_0^2 s + \sigma s \eta - s \eta^2 + F \eta)_x = 0, \quad (2.6)$$

$$s_t + \left(\frac{\sigma}{2} s^2 - s^2 \eta + \eta + F s \right)_x - \tilde{\gamma} v = \tilde{\beta} (D_2 - D_1), \quad (2.7)$$

$$v_t + s v \eta_x + \sigma s v_x - 2 s \eta v_x + F v_x + s V_x + \tilde{\gamma} s = 0, \quad (2.8)$$

$$V_t + (c_0^2 s v + \sigma s v \eta - s v \eta^2 + F V)_x + \tilde{\gamma} F = 0, \quad (2.9)$$

where $\sigma = 2h_1 - 1$, $\tilde{\gamma} = l/L_R$, $L_R = \sqrt{g'H}/f$, $g' = g\Delta\rho/\rho_1$, $\tilde{\beta} = (H/l)^2$.

Next, we consider the Ostrovsky equation regime and assume that $\tilde{\beta} = O(\alpha)$ and $\tilde{\gamma} = O(\alpha^{1/2})$, where α is the small amplitude parameter and scale $\tilde{\beta} = \alpha\beta$, $\tilde{\gamma} = \sqrt{\alpha}\gamma$, where $\beta, \gamma = O(1)$. Then, considering the asymptotic expansions

$$(\eta, s, v, V) = \alpha(\eta, s, v, V)^{(1)} + \alpha^2(\eta, s, v, V)^{(2)} + O(\alpha^3), \quad (2.10)$$

$$F = \alpha F^{(1)} + \alpha^2 F^{(2)} + O(\alpha^3), \quad (2.11)$$

and dropping the terms of $O(\alpha^3)$ (not used in our subsequent derivations), gives the simpler weakly-nonlinear equations

$$\eta_t + c_0^2 s_x = -\alpha(\sigma s \eta + F \eta)_x, \quad (2.12)$$

$$s_t + \eta_x = \sqrt{\alpha}\gamma v - \alpha(\sigma s s_x + F s_x - \frac{\beta c_0^2}{3} s_{xxt}), \quad (2.13)$$

$$v_t = -\sqrt{\alpha}\gamma s - \alpha(\sigma s v_x + F v_x + s V_x), \quad (2.14)$$

$$V_t = -\sqrt{\alpha}\gamma F - \alpha(c_0^2 s v + F V)_x. \quad (2.15)$$

For $F = 0$, the equations reduce to the model derived by Helfrich (2007); Gerkema (1996).

We consider the periodic solutions on the interval $[-L, L]$ (a typical setting for numerical runs using pseudospectral methods). Alongside with the equations (2.12)–(2.15) we will consider the equations for the evolving mean fields by averaging the system with respect to x over this interval and denoting the mean values by hats:

$$\hat{\eta}_t = 0, \quad (2.16)$$

$$\hat{s}_t = \sqrt{\alpha}\gamma\hat{v}, \quad (2.17)$$

$$\hat{v}_t = -\sqrt{\alpha}\gamma\hat{s} - \alpha\frac{1}{2L}\int_{-L}^L(\sigma sv_x + Fv_x + sV_x)dx, \quad (2.18)$$

$$\hat{V}_t = -\sqrt{\alpha}\gamma F. \quad (2.19)$$

Here, the mean fields are generally time-dependent. Hence, the equations for the evolving mean values and deviations from the mean values are generally coupled because of the integral term in the equation (2.18). This significantly differs from our previous derivations of Ostrosky-type equations free from zero-mean contradiction within the scope of Boussinesq-Klein-Gordon equation (Khusnutdinova et al. 2014; Khusnutdinova and Tranter 2019) and coupled Boussinesq equations (Khusnutdinova and Tranter 2022), where the mean fields were described by independent equations.

3. Weakly-nonlinear uni-directional solution free from zero-mean contradiction

In this section, we construct a large class of solutions of the system (2.12)–(2.19) describing uni-directionally propagating waves on top of evolving mean fields by presenting each variable in the form of the sum of its mean value (generally, time-dependent) and deviation from this mean value:

$$\eta = \hat{\eta} + \tilde{\eta}, \quad s = \hat{s} + \tilde{s}, \quad v = \hat{v} + \tilde{v}, \quad V = \hat{V} + \tilde{V}, \quad (3.1)$$

where the unknowns $\hat{\eta}, \hat{s}, \hat{v}, \hat{V}$ and the given function F are assumed to be functions of $t, \tau = \sqrt{\alpha}t, T = \alpha t$, while the deviations $\tilde{\eta}, \tilde{s}, \tilde{v}, \tilde{V}$ are assumed to depend on the fast characteristic variable $\xi = x - c_0t$, where c_0 is the linear long-wave speed, and two slow-time variables τ and T . Both the averages and deviations from the averages are sought in the form of asymptotic multiple-scale expansions in powers of $\sqrt{\alpha}$:

$$(\hat{\eta}, \hat{s}, \hat{v}, \hat{V}) = (\hat{\eta}, \hat{s}, \hat{v}, \hat{V})^{(0)} + \sqrt{\alpha}(\hat{\eta}, \hat{s}, \hat{v}, \hat{V})^{(1)} + \alpha(\hat{\eta}, \hat{s}, \hat{v}, \hat{V})^{(2)} + O(\alpha^{3/2}), \quad (3.2)$$

$$(\tilde{\eta}, \tilde{s}, \tilde{v}, \tilde{V}) = (\tilde{\eta}, \tilde{s}, \tilde{v}, \tilde{V})^{(0)} + \sqrt{\alpha}(\tilde{\eta}, \tilde{s}, \tilde{v}, \tilde{V})^{(1)} + \alpha(\tilde{\eta}, \tilde{s}, \tilde{v}, \tilde{V})^{(2)} + O(\alpha^{3/2}). \quad (3.3)$$

The prescribed function $F(t)$ defining the barotropic transport in the x direction is also assumed to be given in the form

$$F = F^{(0)} + \sqrt{\alpha}F^{(1)} + \alpha F^{(2)} + O(\alpha^{3/2}). \quad (3.4)$$

The average interfacial displacement $\hat{\eta}$ is a constant, and if $\hat{\eta}^{(0)} \neq 0$, then without loss of generality we assume that $\hat{\eta} = \hat{\eta}^{(0)}$. If $\hat{\eta}^{(0)} = 0$, but $\hat{\eta}^{(1)} \neq 0$ then without loss of generality $\hat{\eta} = \sqrt{\alpha}\hat{\eta}^{(1)}$, etc. Similarly, if $F^{(0)} \neq 0$, then we can assume $F = F^{(0)}$, etc.

At $O(1)$ we obtain the equations

$$-c_0\tilde{\eta}_\xi^{(0)} + c_0^2\tilde{s}_\xi^{(0)} = 0, \quad \hat{s}_t^{(0)} - c_0\tilde{s}_\xi^{(0)} + \tilde{\eta}_\xi^{(0)} = 0, \quad (3.5)$$

$$\hat{v}_t^{(0)} - c_0\tilde{v}_\xi^{(0)} = 0, \quad \hat{V}_t^{(0)} - c_0\tilde{V}_\xi^{(0)} = 0, \quad \hat{s}_t^{(0)} = 0, \quad \hat{v}_t^{(0)} = 0, \quad \hat{V}_t^{(0)} = 0, \quad (3.6)$$

implying

$$\hat{s}^{(0)} = A^{(0)}(\tau, T), \quad \hat{v}^{(0)} = B^{(0)}(\tau, T), \quad \hat{V}^{(0)} = C^{(0)}(\tau, T), \quad (3.7)$$

$$\tilde{s}^{(0)} = \frac{1}{c_0} \tilde{\eta}^{(0)}, \quad \tilde{v}^{(0)} = 0, \quad \tilde{V}^{(0)} = 0. \quad (3.8)$$

Here, the functions $(A, B, C)^{(0)}$ are arbitrary functions of their variables, and we have used that all deviations should have zero mean, by construction of the solution.

Next, collecting the terms of order $O(\sqrt{\alpha})$, using relations (3.7), (3.8) and simplifying the resulting system by virtue of its averaged members, we obtain the system

$$-c_0 \tilde{\eta}_\xi^{(1)} + c_0^2 \tilde{s}_\xi^{(1)} = -\tilde{\eta}_\tau^{(0)}, \quad -c_0 \tilde{s}_\xi^{(1)} + \tilde{\eta}_\xi^{(1)} = -\frac{1}{c_0} \tilde{\eta}_\tau^{(0)}, \quad (3.9)$$

$$\tilde{v}_\xi^{(1)} = \frac{\gamma}{c_0^2} \tilde{\eta}^{(0)}, \quad \tilde{V}_\xi^{(1)} = 0, \quad (3.10)$$

$$\hat{s}_t^{(1)} = \gamma B^{(0)} - A_\tau^{(0)}, \quad \hat{v}_t^{(1)} = -\gamma A^{(0)} - B_\tau^{(0)}, \quad \hat{V}_t^{(1)} = -\gamma F^{(0)} - C_\tau^{(0)}. \quad (3.11)$$

Equations (3.9) imply

$$\tilde{\eta}_\tau^{(0)} = 0, \quad \tilde{s}^{(1)} = \frac{1}{c_0} \tilde{\eta}^{(1)}, \quad (3.12)$$

again using that all deviations have zero mean.

To avoid secular growth in $\hat{s}^{(1)}$ and $\hat{v}^{(1)}$, we require that

$$A_\tau^{(0)} = \gamma B^{(0)}, \quad B_\tau^{(0)} = -\gamma A^{(0)}, \quad (3.13)$$

which implies $A_{\tau\tau}^{(0)} = -\gamma^2 A^{(0)}$, yielding

$$A^{(0)} = A(T) \cos \gamma[\tau + \phi(T)], \quad B^{(0)} = -A(T) \sin \gamma[\tau + \phi(T)], \quad (3.14)$$

where $A(T)$ and $B(T)$ are arbitrary functions of T .

To avoid secular growth in $\hat{V}^{(1)}$ one can consider two options:

(i) $F^{(0)} = F^{(0)}(\tau, T)$, then $C_\tau^{(0)} = -\gamma F^{(0)}$, implying

$$\hat{V}^{(0)} = C^{(0)} = -\gamma \int_0^\tau F^{(0)}(\tilde{\tau}, T) d\tilde{\tau}; \quad (3.15)$$

(ii) $F^{(0)} = F^{(0)}(t, \tau, T)$ such that $\hat{V}^{(1)} = -\int_0^t [\gamma F^{(0)}(t, \tau, T) + C_\tau^{(0)}(\tau, T)] d\tilde{\tau}$ is bounded, e.g. $F^{(0)} = -C_\tau^{(0)} + \sin \omega t$, where $\omega = \omega(\tau, T)$.

In what follows, we consider the first case. Then, summarising, we have

$$\hat{s}^{(0)} = A(T) \cos \gamma[\tau + \phi(T)], \quad \hat{v}^{(0)} = -A(T) \sin \gamma[\tau + \phi(T)], \quad (3.16)$$

$$\hat{V}^{(0)} = -\gamma \int_0^\tau F^{(0)}(\tilde{\tau}, T) d\tilde{\tau}, \quad \tilde{s}^{(0)} = \frac{1}{c_0} \tilde{\eta}^{(0)}(\xi, T), \quad \tilde{v}^{(0)} = 0, \quad \tilde{V}^{(0)} = 0; \quad (3.17)$$

$$\hat{s}^{(1)} = A^{(1)}(\tau, T), \quad \hat{v}^{(1)} = B^{(1)}(\tau, T), \quad \hat{V}^{(1)} = C^{(1)}(\tau, T), \quad \tilde{s}^{(1)} = \frac{1}{c_0} \tilde{\eta}^{(1)}, \quad (3.18)$$

$$\tilde{v}^{(1)} = \frac{\gamma}{c_0^2} \left(\int_{-L}^\xi \tilde{\eta}^{(0)}(\tilde{\xi}, T) d\tilde{\xi} - \left\langle \int_{-L}^\xi \tilde{\eta}^{(0)}(\tilde{\xi}, T) d\tilde{\xi} \right\rangle \right), \quad \tilde{V}^{(1)} = 0. \quad (3.19)$$

Here, $\left\langle \int_{-L}^\xi \tilde{\eta}^{(0)}(\tilde{\xi}, T) d\tilde{\xi} \right\rangle = \frac{1}{2L} \int_{-L}^L \left(\int_{-L}^\xi \tilde{\eta}^{(0)}(\tilde{\xi}, T) d\tilde{\xi} \right) d\xi$ is the mean value.

Finally, collecting the terms at $O(\alpha)$, using (3.16)–(3.19) and simplifying the resulting

system by virtue of its averaged members, we obtain

$$-c_0\tilde{\eta}_\xi^{(2)} + c_0^2\tilde{s}_\xi^{(2)} = -\frac{\sigma}{c_0}(\hat{\eta}^{(0)} + \tilde{\eta}^{(0)})\tilde{\eta}_\xi^{(0)} - \sigma \left(A(T) \cos \gamma[\tau + \phi(T)] + \frac{1}{c_0}\tilde{\eta}^{(0)} \right) \tilde{\eta}_\xi^{(0)} - F^{(0)}\tilde{\eta}_\xi^{(0)} - \tilde{\eta}_\tau^{(1)} - \tilde{\eta}_T^{(0)}, \quad (3.20)$$

$$-c_0\tilde{s}_\xi^{(2)} + \tilde{\eta}_\xi^{(2)} = \frac{\gamma}{c_0^2} \left(\int_{-L}^{\xi} \tilde{\eta}^{(0)}(\tilde{\xi}, T) d\tilde{\xi} - \left\langle \int_{-L}^{\xi} \tilde{\eta}^{(0)}(\tilde{\xi}, T) d\tilde{\xi} \right\rangle \right) - \frac{\beta c_0^2}{3} \tilde{\eta}_{\xi\xi\xi}^{(0)} - \sigma \left(A(T) \cos \gamma[\tau + \phi(T)] + \frac{1}{c_0}\tilde{\eta}^{(0)} \right) \tilde{\eta}_\xi^{(0)} - \frac{1}{c_0} (F^{(0)}\tilde{\eta}_\xi^{(0)} - \tilde{\eta}_\tau^{(1)} - \tilde{\eta}_T^{(0)}), \quad (3.21)$$

$$\tilde{v}_\xi^{(2)} = \frac{\gamma}{c_0^2} \tilde{\eta}^{(1)} - \frac{1}{c_0} (A_T \sin \gamma[\tau + \phi(T)] + \gamma A \phi_T \cos \gamma[\tau + \phi(T)]), \quad (3.22)$$

$$\tilde{V}_\xi^{(2)} = -A(T) \sin \gamma[\tau + \phi(T)] \tilde{\eta}_\xi^{(0)} - \frac{\gamma}{c_0} \int_0^\tau F_T^{(0)}(\tilde{\tau}, T) d\tilde{\tau}, \quad (3.23)$$

$$\hat{s}_\tau^{(2)} = \gamma B^{(1)} - A_\tau^{(1)} - A_T \cos \gamma[\tau + \phi(T)] + \gamma A \phi_T \sin \gamma[\tau + \phi(T)], \quad (3.24)$$

$$\hat{v}_\tau^{(2)} = -\gamma A^{(1)} - B_\tau^{(1)} + A_T \sin \gamma[\tau + \phi(T)] + \gamma A \phi_T \cos \gamma[\tau + \phi(T)], \quad (3.25)$$

$$\hat{V}_\tau^{(2)} = -\gamma F^{(1)} - C_\tau^{(1)} + \gamma \int_0^\tau F_T^{(0)}(\tilde{\tau}, T) d\tilde{\tau}. \quad (3.26)$$

Equations (3.20) and (3.21) yield the equation

$$2\tilde{\eta}_T^{(0)} + \left[\frac{\sigma\hat{\eta}^{(0)}}{c_0} + 2\sigma A \cos \gamma(\tau + \phi) + 2F^{(0)}(\tau, T) \right] \tilde{\eta}_\xi^{(0)} + \frac{3\sigma}{c_0} \tilde{\eta}^{(0)} \tilde{\eta}_\xi^{(0)} + \frac{\beta c_0^3}{3} \tilde{\eta}_{\xi\xi\xi}^{(0)} - \frac{\gamma^2}{c_0} \left(\int_{-L}^{\xi} \tilde{\eta}^{(0)}(\tilde{\xi}, T) d\tilde{\xi} - \left\langle \int_{-L}^{\xi} \tilde{\eta}^{(0)}(\tilde{\xi}, T) d\tilde{\xi} \right\rangle \right) + 2\tilde{\eta}_\tau^{(1)} = 0. \quad (3.27)$$

Differentiating equation (3.27) with respect to τ , we obtain

$$\tilde{\eta}_\tau^{(1)} = -[\sigma A \cos \gamma(\tau + \phi) - F^{(0)}] \tilde{\eta}_\xi^{(0)}, \quad (3.28)$$

which yields, using that the function should have zero mean,

$$\tilde{\eta}^{(1)} = - \left[\frac{\sigma A}{\gamma} \sin \gamma(\tau + \phi) + \int_0^\tau F^{(0)}(\tilde{\tau}, T) d\tilde{\tau} \right] \tilde{\eta}_\xi^{(0)}. \quad (3.29)$$

Then, using (3.29), equation (3.28) yields the Ostrovsky equation in the form

$$2\tilde{\eta}_T^{(0)} + \frac{\sigma\hat{\eta}^{(0)}}{c_0} \tilde{\eta}_\xi^{(0)} + \frac{3\sigma}{c_0} \tilde{\eta}^{(0)} \tilde{\eta}_\xi^{(0)} + \frac{\beta c_0^3}{3} \tilde{\eta}_{\xi\xi\xi}^{(0)} - \frac{\gamma^2}{c_0} \left(\int_{-L}^{\xi} \tilde{\eta}^{(0)}(\tilde{\xi}, T) d\tilde{\xi} - \left\langle \int_{-L}^{\xi} \tilde{\eta}^{(0)}(\tilde{\xi}, T) d\tilde{\xi} \right\rangle \right) = 0. \quad (3.30)$$

Differentiating with respect to ξ and changing the variable ξ to $\zeta = \xi - \frac{\sigma\hat{\eta}^{(0)}}{2c_0}T$ leads to the traditional form

$$\left(\tilde{\eta}_T^{(0)} + \alpha_1 \tilde{\eta}^{(0)} \tilde{\eta}_\zeta^{(0)} + \beta_1 \tilde{\eta}_{\zeta\zeta\zeta}^{(0)} \right)_\zeta = \gamma_1 \tilde{\eta}^{(0)}, \quad (3.31)$$

where

$$\alpha_1 = \frac{3\sigma}{2c_0}, \quad \beta_1 = \frac{\beta c_0^3}{6}, \quad \gamma_1 = \frac{\gamma^2}{2c_0}.$$

Next, substituting equation (3.29) for $\tilde{\eta}^{(1)}$ in equation (3.22) for $\tilde{v}_\xi^{(2)}$ and requiring that there is no secular growth in $\tilde{v}^{(2)}$, and that the function has zero mean, we conclude that

$$A_T = 0, \quad \phi_T = 0, \quad \tilde{v}^{(2)} = - \left[\frac{\sigma A}{c_0^2} \sin \gamma(\tau + \phi) + \frac{\gamma}{c_0^2} \int_0^\tau F^{(0)}(\tilde{\tau}, T) d\tilde{\tau} \right] \tilde{\eta}^{(0)}. \quad (3.32)$$

Similarly, equation (3.24) yields

$$F_T^{(0)} = 0, \quad \text{and} \quad \tilde{V}^{(2)} = -A \sin \gamma(\tau + \phi) \tilde{\eta}^{(0)}. \quad (3.33)$$

Finally, the equations for the mean values simplify to take the form

$$\hat{s}_t^{(2)} = \gamma B^{(1)} - A_\tau^{(1)}, \quad \hat{v}_t^{(2)} = -\gamma A^{(1)} - B_\tau^{(1)}, \quad \hat{V}_t^{(2)} = -\gamma F^{(1)} - C_\tau^{(1)}. \quad (3.34)$$

Assuming that $F^{(1)} = F^{(1)}(\tau, T)$, we then have

$$A_\tau^{(1)} = \gamma B^{(1)}, \quad B_\tau^{(1)} = -\gamma A^{(1)}, \quad C_\tau^{(1)} = -\gamma F^{(1)}, \quad (3.35)$$

yielding similar conclusions to those for $(A, B, C)^{(0)}$. In what follows, we consider $(F, A, B, C)^{(1)} = 0$.

Hence, considering the equations up to $O(\alpha)$, i.e. up to the accuracy of the governing equations (2.12)–(2.19), allows us to fully define all terms at $O(1)$ and $O(\sqrt{\alpha})$. The procedure can be continued to any order, but instead of using the truncated weakly-nonlinear formulation, we would need to use the original strongly-nonlinear equations.

To summarise, up to the accuracy of the governing equations, we obtained the following large class of uni-directional waves described by the Ostrovsky equation and propagating over the non-zero, generally evolving, mean fields:

$$\eta = \hat{\eta}^{(0)} + \tilde{\eta}^{(0)} - \sqrt{\alpha} \left[\frac{\sigma A}{\gamma} \sin \gamma(\tau + \phi) + \int_0^\tau F^{(0)}(\tilde{\tau}) d\tilde{\tau} \right] \tilde{\eta}_\xi^{(0)} + O(\alpha), \quad (3.36)$$

$$s = A \cos \gamma(\tau + \phi) + \frac{1}{c_0} \tilde{\eta}^{(0)} - \sqrt{\alpha} \frac{1}{c_0} \left[\frac{\sigma A}{\gamma} \sin \gamma(\tau + \phi) + \int_0^\tau F^{(0)}(\tilde{\tau}) d\tilde{\tau} \right] \tilde{\eta}_\xi^{(0)} + O(\alpha), \quad (3.37)$$

$$v = -A \sin \gamma(\tau + \phi) + \sqrt{\alpha} \frac{\gamma}{c_0^2} \left[\int_{-L}^\zeta \tilde{\eta}^{(0)}(\tilde{\zeta}, T) d\tilde{\zeta} - \left\langle \int_{-L}^\zeta \tilde{\eta}^{(0)}(\tilde{\zeta}, T) d\tilde{\zeta} \right\rangle \right] + O(\alpha), \quad (3.38)$$

$$V = -\gamma \int_0^\tau F^{(0)}(\tilde{\tau}) d\tilde{\tau} + O(\alpha), \quad (3.39)$$

where $\hat{\eta}^{(0)}$, A , ϕ are arbitrary constants, $F^{(0)}(\tilde{\tau})$ is a function such that $\int_0^\tau F^{(0)}(\tilde{\tau}) d\tilde{\tau}$ is bounded (e.g. $\sin \omega \tilde{\tau}$), and $\tilde{\eta}^{(0)} = \tilde{\eta}^{(0)}(\zeta, T)$ satisfies the Ostrovsky equation (3.31), where

$$\zeta = \xi - \frac{\sigma \hat{\eta}^{(0)}}{2c_0} T = x - \left(c_0 + \frac{\alpha \sigma \hat{\eta}^{(0)}}{2c_0} \right) t, \quad T = \alpha t. \quad (3.40)$$

We note that the function $\tilde{\eta}^{(0)}$ has zero mean by construction, η has a constant mean value,

while the shear variables s and v generally have time-dependent mean values. The barotropic transport variables F and V are also generally time-dependent. In the rest of this paper we consider the case $F^{(0)} = 0$ (i.e., the barotropic transport is absent).

4. The effect of rotation on the evolution of cnoidal waves with defects

The aim of this section is to model the evolution of the waves generated by initial conditions close to the cnoidal waves of the KdV equation but having local amplitude and/or periodicity defects. We use the weakly-nonlinear solution constructed in Section 3 and first model the effect of rotation on the exact classical solutions of the KdV equation: solitons and cnoidal waves (Boussinesq 1871; Korteweg and de Vries 1895), as well as bright and dark breathers (Kuznetsov & Mikhailov 1975; Hoefler et al. 2023). Then, we consider cnoidal waves with the local contraction and expansion periodicity defects introduced by symmetrically cutting away a part close to the trough between the two neighbouring peaks and gluing together the remaining parts of the solution, and by cutting at the trough and symmetrically inserting a piece of a straight line, respectively (see the first two rows in Figure 17 of the Appendix A). This allows us to set up a framework for the discussion of the effects observed in our subsequent modelling of cnoidal waves with generic localised defects. As a by-product of our study of initial conditions with local periodicity defects we came across an observation that these functions are in fact weak solutions of the KdV equation. In Appendix A, we prove that all conservation laws of the KdV equation (infinitely many) are identically satisfied for them. Moreover, the expansion defect has a smooth first derivative.

In our numerical experiments, we use two sets of parameters. In the first set, which is used for the majority of our simulations (except the runs shown in Figures 13, 14 (right) and 15 (right)), the pycnocline is closer to the surface, and internal waves are the waves of depression. Hence, we show the bottom view in the majority of our figures in this section. The depths of the upper and lower layers are 37.5 m and 112.5 m, respectively, and the total depth of the system, denoted by H , is 150.0 m. The densities of the upper and lower layers are chosen to be $\rho_1 = 1000.0$, $\rho_2 = 1003.1 \text{ kg m}^{-3}$, respectively. The small parameters are defined as $\alpha = a/H$, $\tilde{\beta} = (H/l)^2$ and $\tilde{\gamma} = (lf)/\sqrt{(g'H)}$, where a is a wave amplitude, l is a wavelength, f is the Coriolis parameter, $g' = g\Delta\rho/\rho_1$ is the reduced gravity. We let $\alpha = 0.005$ and $\tilde{\beta} = 0.030$. We assume midlatitude oceanic values for the Coriolis parameter $f = 5 \times 10^{-5} \text{ s}^{-1}$, and reduced gravity $g' = 0.030 \text{ m s}^{-2}$. Hence, $\tilde{\gamma} \approx 0.020$. The non-dimensional unperturbed upper layer depth $h_0 = 0.250$ gives values of the linear long wave speed $c_0 = (h_0 - h_0^2)^{1/2} \approx 0.433$ and coefficient $\sigma = 2h_0 - 1 = -0.500$. The scaled $\mathcal{O}(1)$ parameters are $\beta = \tilde{\beta}/\alpha$ and $\gamma = \tilde{\gamma}/\sqrt{\alpha}$. Then, the coefficients of the Ostrovsky equation (3.31) are given by $\alpha_1 \approx -1.732$, $\beta_1 \approx 0.081$, $\gamma_1 \approx 0.096$. This regime is close to one of the regimes considered by Helfrich (2007), and internal waves are waves of depression. The second set of parameters is used to model the internal waves of elevation shown in Figures 13, 14 (right) and 15 (right), and here the pycnocline is closer to the bottom: the depths of the upper and lower layers are 120.0 and 30.0 m, respectively. The total depth of the system is again $H = 150.0$ m. The other parameters are unchanged except the non-dimensional unperturbed upper layer depth $h_0 = 0.800$, giving values of the linear long wave speed $c_0 = (h_0 - h_0^2)^{1/2} = 0.400$ and coefficient $\sigma = 2h_0 - 1 = 0.600$. Then, the coefficients of the Ostrovsky equation (3.31) are found to be $\alpha_1 = 2.250$, $\beta_1 = 0.064$, $\gamma_1 \approx 0.104$. The Ostrovsky equation is solved using a pseudospectral method described in Appendix B. Parameters specifying the inertial oscillations (“twitching”) are chosen to be $A = 1$ and $\phi = 0$, and $A = 0$ in the KdV regime (no rotation).

4.1. The effect of rotation on solitons and cnoidal waves

We begin by modelling the evolution of initial conditions in the form of solitary and cnoidal wave solutions of the KdV equation associated with the Ostrovsky equation (3.31):

$$\tilde{\eta}_T^{(0)} + \alpha_1 \tilde{\eta}^{(0)} \tilde{\eta}_\zeta^{(0)} + \beta_1 \tilde{\eta}_\zeta \tilde{\eta}_\zeta^{(0)} = 0. \quad (4.1)$$

Hence, at $T = 0$ the initial condition for the Ostrovsky equation (3.31) corresponding to the soliton solution is given by the mean-free part of the function

$$\tilde{\eta}^{(0)} = \frac{3v_s}{\alpha_1} \operatorname{sech}^2 \left[\frac{1}{2} \sqrt{\frac{v}{\beta_1}} (\zeta - v_s T - \zeta_0) \right]_{T=0}, \quad (4.2)$$

where ζ_0 and $v_s > 0$ are arbitrary constants, while the initial condition for the Ostrovsky equation (3.31) corresponding to the cnoidal wave of equation (4.1) takes the form of the mean-free part of the solution given in terms of the Jacobi elliptic functions by

$$\tilde{\eta}^{(0)} = \frac{6\beta_1}{\alpha_1} \left\{ u_2 + (u_3 - u_2) \operatorname{cn}^2 \left[(\zeta - v_c T) \sqrt{\frac{u_3 - u_1}{2}}; m \right] \right\}_{T=0}, \quad (4.3)$$

where $u_1 < u_2 < u_3$ are real, $v_c = 2\beta_1(u_1 + u_2 + u_3)$, and $m = (u_3 - u_2)/(u_3 - u_1)$ is the elliptic modulus. In the limit $m \rightarrow 1$, the cnoidal wave approaches a soliton (generally, on a non-zero pedestal). The period of the cnoidal wave is given by

$$\lambda = \frac{2K(m)}{\sqrt{(u_3 - u_1)/2}}, \quad (4.4)$$

where $K(m)$ is the complete elliptic integral of the first kind (see, for example, Kamchatnov 2000).

In Figure 3, we compare the evolution of a single soliton in a two-layer fluid system with rotation in numerical experiments with periodic boundary conditions, either with or without the sponge layers near the boundaries (see, for example, Alias et al. 2013 for the discussion of the sponge layers). The sponge layers near the boundaries act as a filter absorbing the radiation. The computational domain is $2L = 100$, with the number of modes $M = 998$, the spatial step $\Delta x \approx 10^{-1}$, the total simulation time $T_{max} = 200$, and the temporal step $\Delta T = 10^{-2}$. Other constants are $v_s \approx 0.487$ and $\zeta_0 = 0$.

Top row of Figure 3 shows three-dimensional plots of the time evolution of the interfacial displacement for initial conditions in the form of a single soliton, without (left) and with (right) the sponge layers near the boundaries of the periodic domain. The soliton evolves into a wavepacket as it propagates, and for a long time the radiation penetrating through the boundaries in the absence of sponge layers does not have a large effect on the shape or speed of the main wavepacket, which is shown in more detail in the middle and bottom rows of Figure 3. The overall wave pattern remains stable and consistent throughout the simulation.

Similarly, in Figure 4 we show the effect of rotation on the cnoidal wave initial condition. The computational domain is $2L = 26.40$, with the number of modes $M = 262$, the spatial step $\Delta x \approx 10^{-1}$, the total simulation time $T_{max} = 100$, and the temporal step $\Delta T = 10^{-2}$. The parameters characterising the initial condition are $u_1 = -10^{-3}$, $u_2 = 0$ and $u_3 = 3$. It is evident that rotation leads to formation of a rather regular quasi-periodic wave pattern shown in Figure 4, without the formation of bursts of large waves.

We also note that both for the soliton and cnoidal wave initial conditions the time evolution of the maximum and minimum of the free-surface elevation is quasi-periodic, with no significant bursts, as shown in Figure 5. All computational parameters are the same as in the

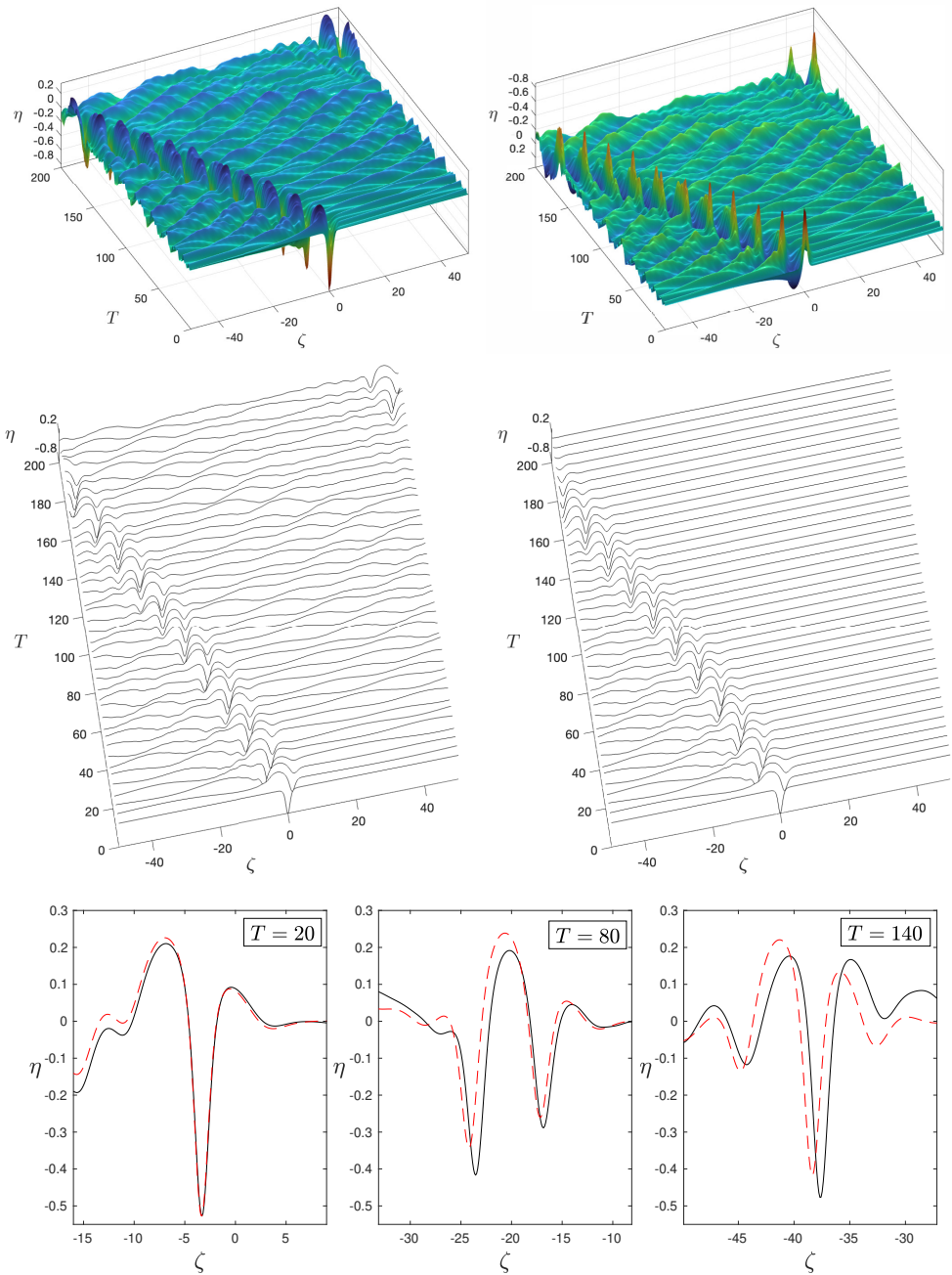


Figure 3: The effect of rotation on the KdV soliton initial condition in simulations with periodic boundary conditions. First row: view from above (left) and view from below (right) of the interfacial displacement. Second row: interfacial displacement in simulations without the sponge layers (left) and with the sponge layers (right). Third row: comparison of the lead wavepacket in simulations without the sponge layers (black) and with the sponge layers (red dashed).

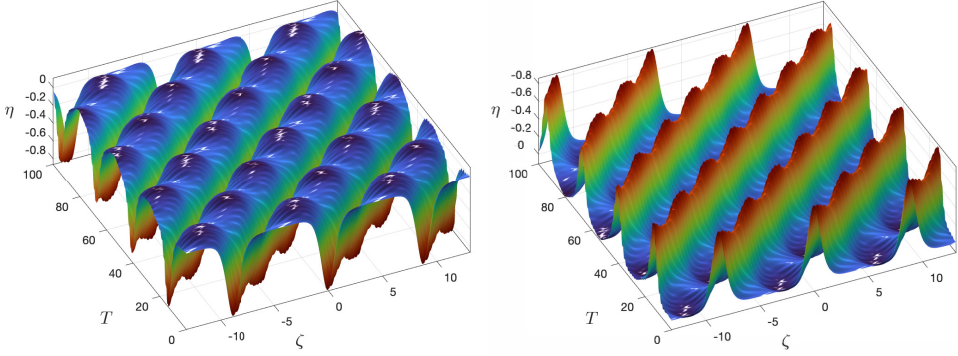


Figure 4: The effect of rotation on the KdV cnoidal wave initial condition: view from above (left) and view from below (right) of the interfacial displacement.

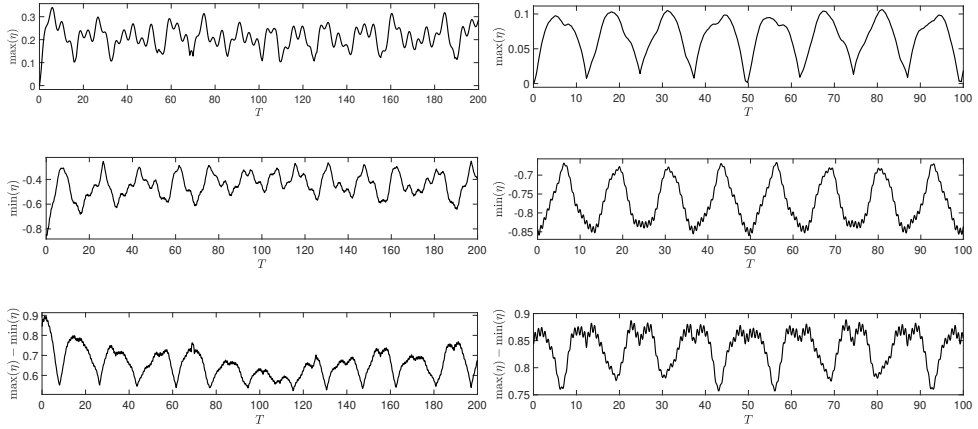


Figure 5: Evolution of the maximum, minimum and amplitude of the interfacial displacement for a soliton (left) and cnoidal wave (right) initial condition on a periodic domain under the effect of rotation.

previous figures. Hence, we conclude that rotation alone does not trigger formation of large waves in these simulations.

4.2. The effect of rotation on breathers on a cnoidal wave background

The exact breather on a cnoidal wave solutions of the KdV equation were studied by Kuznetsov & Mikhailov (1975); Hoefler et al. (2023). There are two types of breathers: bright and dark (this terminology refers to the canonical form of the KdV equation, where solitons are waves of elevation). For a bright breather propagating as a dislocation of a cnoidal wave the exact solution of the KdV equation (4.1) takes the form

$$\tilde{\eta}^{(0)} = \frac{12\beta_1}{\alpha_1} \left\{ k^2 - 1 + \frac{E(k)}{K(k)} + \frac{\partial^2}{\partial \zeta^2} \left[\log(\tau(\zeta, \beta_1 T)) \right] \right\}, \quad (4.5)$$

where $k \in (0, 1)$ is the elliptic modulus (the elliptic parameter $m = k^2$), $K(k)$ is the complete elliptic integral of the first kind, $E(k)$ is the complete elliptic integral of the second kind, and the τ -function is given by

$$\tau(x, t) := \Theta(x - c_0 t + \alpha_b) \exp\{\kappa_b(x - c_b t + x_0)\} + \Theta(x - c_0 t - \alpha_b) \exp\{-\kappa_b(x - c_b t + x_0)\}$$

with $\kappa_b > 0$, $c_b > c_0$ and $\alpha_b \in (0, K(k))$. Here, $\Theta(x) = \theta_4\left(\frac{\pi x}{2K(k)}\right)$, where θ_4 is the Jacobi theta function of type four, given by $\theta_4(u) = 1 + 2 \sum_{n=1}^{\infty} (-1)^n q^{n^2} \cos(2nu)$. The solution is parameterised by $\lambda \in (-\infty, -k^2)$. The parameters are defined as follows (Hoefler et al. 2023):

$$\varphi_\gamma = \arcsin\left(\frac{\sqrt{-\lambda - k^2}}{\sqrt{1 - 2k^2 - \lambda}}\right), \quad (4.6)$$

$$\alpha_b = F(\varphi_\gamma, k), \quad \kappa_b = \frac{\sqrt{1 - \lambda - k^2}\sqrt{-\lambda - k^2}}{\sqrt{1 - 2k^2 - \lambda}} - Z(\varphi_\gamma, k), \quad (4.7)$$

$$c_0 = 4(2k^2 - 1), \quad c_b = c_0 + \frac{4\sqrt{1 - \lambda - 2k^2}\sqrt{1 - \lambda - k^2}\sqrt{-\lambda - k^2}}{\kappa_b}, \quad (4.8)$$

where $F(\varphi, k) := \int_0^\varphi \frac{d\theta}{\sqrt{1 - k^2 \sin^2 \theta}}$ is the elliptic integral of the first kind, and $Z(\varphi, k) := \int_0^\varphi \sqrt{1 - k^2 \sin^2 \theta} d\theta$ is the elliptic integral of the second kind.

For a dark breather propagating as a dislocation of a cnoidal wave the exact solution is again given by equation (4.5), where the solution is now parameterised by $\lambda \in (1 - 2k^2, 1 - k^2)$, and the τ -function takes the form

$$\tau(x, t) := \Theta(x - c_0 t + \alpha_d) \exp\{-\kappa_d(x - c_d t + x_0)\} + \Theta(x - c_0 t - \alpha_d) \exp\{\kappa_d(x - c_d t + x_0)\}$$

with $\kappa_d > 0$, $c_d < c_0$ and $\alpha_d \in (0, K(k))$. The parameters are given by

$$\varphi_\alpha = \arcsin\left(\frac{\sqrt{1 - k^2 - \lambda}}{k}\right), \quad (4.9)$$

$$\alpha_d = F(\varphi_\alpha, k), \quad \kappa_d = Z(\varphi_\alpha, k), \quad (4.10)$$

$$c_0 = 4(2k^2 - 1), \quad c_d = c_0 - \frac{4\sqrt{(k^2 + \lambda)(\lambda - 1 + 2k^2)(1 - k^2 - \lambda)}}{\kappa_d}. \quad (4.11)$$

Numerical solutions initiated with the bright and dark breather on a cnoidal wave initial conditions in the absence of rotation are shown in the first row of Figure 6. For the bright breather simulations, shown in the left column, the computational domain length is $2L = 72.86$, with the number of modes $M = 728$, the spatial step $\Delta x \approx 10^{-1}$, the total simulation time $T_{max} = 100$, and the temporal step $\Delta T = 10^{-2}$. The parameters used in the initial condition are $[k, \lambda] \approx [0.9998, -1.30]$. For the dark breather simulations, shown in the right column, the computational domain length is $2L = 80.64$, with the number of modes $M = 804$, the spatial step $\Delta x \approx 10^{-1}$, the total simulation time $T_{max} = 100$, and the temporal step $\Delta T = 10^{-2}$. The other parameters are $[k, \lambda] \approx [0.9998, -0.50]$. In the absence of rotation, the plots show stable propagation of the bright and dark breather solutions on top of the cnoidal wave, in full agreement with the available analytical solution (4.5).

Next, the effect of rotation on the evolution of the bright breather on a cnoidal wave initial condition is shown in the subsequent rows of the same Figure 6, for the interfacial displacement (second row), shear in the direction of wave propagation (third row) and shear in the orthogonal direction (fourth row). We notice a striking difference with the results shown in the top row of the figure (no rotation): there emerges a rather strong left-propagating localised burst clearly visible both in the free surface elevation (second row) and the shear in the direction of wave propagation (third row). The counterpart of the wave is also present in the shear in the orthogonal direction (fourth row), but this signal is weak. It must be noted that the wave forms soon after the initiation of the simulation, and it continues to grow for a long time.

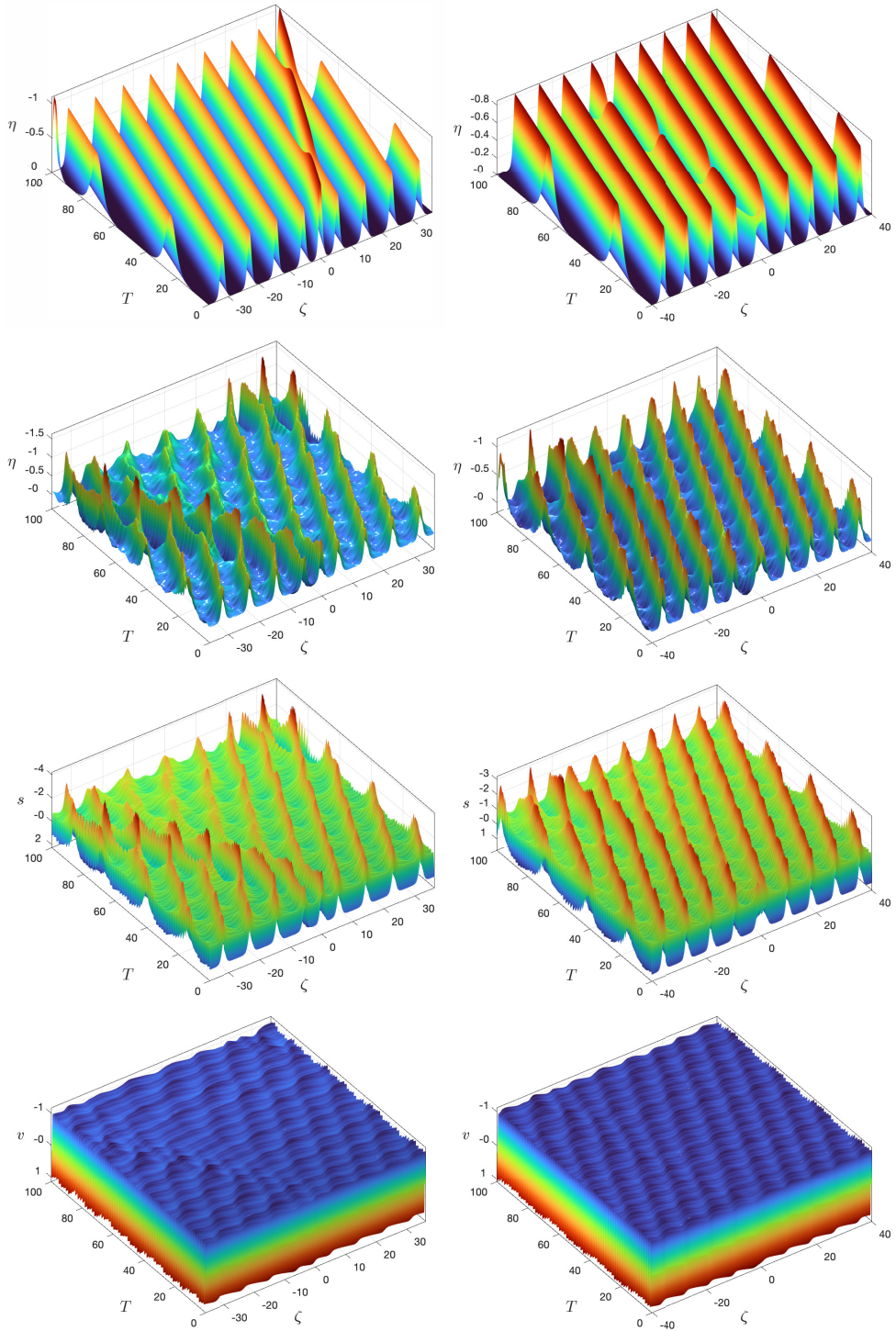


Figure 6: Numerical solution for a bright (left) and dark (right) breather on a cnoidal wave initial condition (view from below). First row: interfacial displacement in the absence of rotation. Second row: interfacial displacement under the effect of rotation. Third / fourth row: shear in the direction of wave propagation / orthogonal direction, under the effect of rotation.

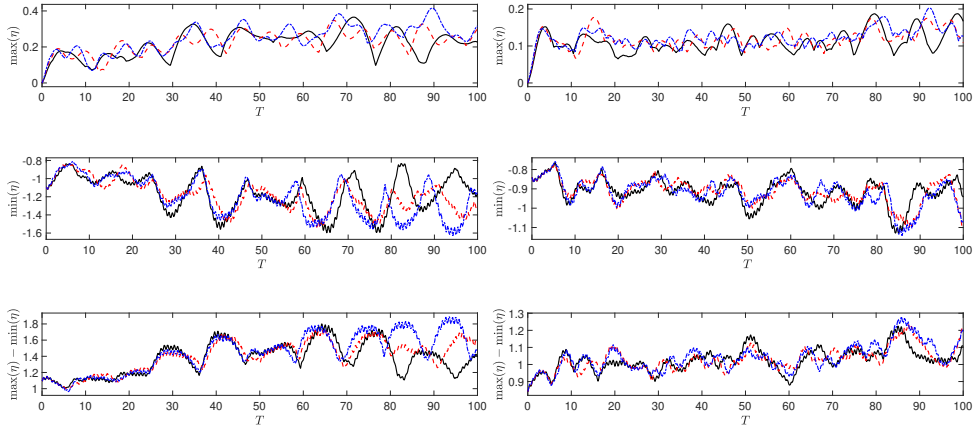


Figure 7: The effect of rotation on the evolution of the maximum, minimum and amplitude of the interfacial displacement for a bright (left) and dark (right) breather on a cnoidal wave initial condition. Black solid, red dashed and blue dot-dashed lines correspond to 5, 7 and 9 peaks in the domain, respectively.

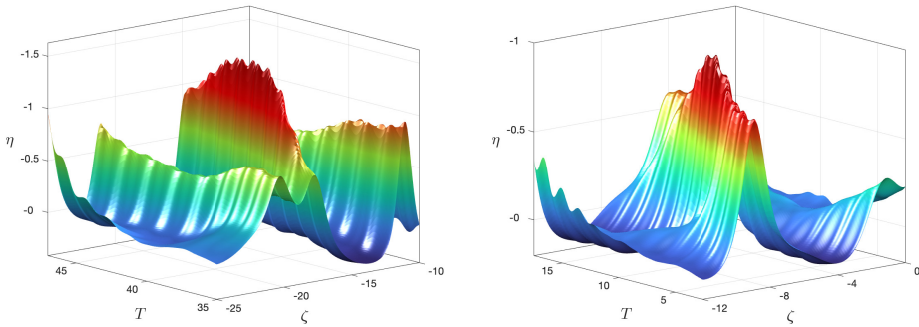


Figure 8: Close-up view from below of the large burst in the interfacial displacement for a bright (left) and dark (right) breather on a cnoidal wave initial condition around $T = 40$ (left) and $T = 10$ (right), respectively.

In these runs, the effect on a dark breather on a cnoidal wave is qualitatively similar to that on the bright breather, though less pronounced. In both cases, the background cnoidal wave continues propagating to the right (in the moving reference frame), and there appears a significant burst both in the interfacial displacement and the shear in the direction of wave propagation, moving to the left. For the dark breather, the signal in the shear in the orthogonal direction is also present, but it is barely noticeable to the naked eye.

Figure 7 shows the time evolution of the maximum, minimum and the amplitude of the interfacial displacement for both cases of a bright (left column) and dark (right column) breather on a cnoidal wave initial condition. We see that the observed effects of rotation are structurally stable with regard to the size of the computational domain. We experimented with 5, 7 and 9 major peaks in the domain. In the bright-breather case, the computational domains are $2L = 37.42$ (5 peaks), $2L = 55.02$ (7 peaks), $2L = 72.86$ (9 peaks). For the dark-breather case, the computational domains are $2L = 45.44$ (5 peaks), $2L = 63.04$ (7 peaks), $2L = 80.64$ (9 peaks). The remaining numerical parameters are the same as before. It is again evident that the wave amplitude grows. The burst forms soon after the initiation of the numerical runs. The close-up views of the large waves visible in the free surface elevation are

shown in Figure 8 for the time around $T = 40$ (bright breather case, left) with approximately 32% increase in the amplitude compared to the initial condition, and around $T = 10$ (dark breather case, right) with approximately 18% increase in the amplitude compared to the initial condition. Hence, we conclude that under the effect of rotation the moving dislocation on top of the otherwise regular cnoidal wave can lead to the emergence of strong bursts of interfacial waves and shear currents in the direction of propagation of the cnoidal wave.

4.3. *The effect of rotation on cnoidal waves with periodicity defects*

Recent research related to the wave packets described by the Schrödinger equation has shown that localised phase defects can lead to the emergence of rogue waves (He et al. 2022). Here, we investigate whether periodicity defects introduced into the long cnoidal waves in the KdV-Ostrovsky regime can also lead to the emergence of large localised bursts of energy, under the effect of rotation. Also, can it happen already in the absence of rotation, i.e. in the KdV regime?

Motivated by Figure 1, we consider cnoidal waves close to their solitonic limit and introduce two types of periodicity defects (see Figure 17 in Appendix A): contraction and expansion defects, depending on whether the distance between the two neighbouring peaks is shorter or longer than the period of the cnoidal wave. The first defect is introduced by symmetrically cutting away a small part close to the trough between the two neighbouring peaks, and gluing together the remaining parts of the solution. Naturally, the resulting function has discontinuous derivative at one point within the computational domain, but the jump in the derivative is small because we have cut close to extremum (smoothed in numerical simulations). The second defect is introduced by cutting the graph at the trough and symmetrically inserting a piece of a straight line. The resulting function has continuous first derivative. To our surprise, these functions evolved almost like travelling waves of the KdV equation. Both types of waves were long-lived, and cnoidal wave with an expansion defect was stable, with no visible changes at the end of the long run. The numerical results initiated with such initial conditions in the absence of rotation are shown in the first row of Figure 9 for the contraction defect (left column) and the expansion defect (right column). Intrigued by this observation, we managed to prove that for the constructed functions (and their natural generalisations) all (infinitely many) conservation laws of the KdV equation are satisfied exactly. This approach was inspired by the recent work by Gavriluk et al. (2020); Gavriluk and Shyue (2022); Gavriluk et al. (2024), where some solutions with singularities satisfying the Weierstrass–Erdmann corner conditions (e.g. Fox 1954) and requiring the continuity of the derivative at the junction, were constructed in the context of non-integrable Benjamin–Bona–Mahoney and conduit equations. To the best of our knowledge, the discontinuous travelling wave solutions of the KdV equation in the form of cnoidal waves with periodicity defects constructed in our paper have not been discussed before. A cnoidal wave with an expansion defect satisfies the corner condition exactly and is a weak solution of the KdV equation, its smoothed counterpart was extremely stable in our numerical runs, but a smoothed counterpart of a cnoidal wave with a contraction defect also turned out to be long-lived, and could be viewed as an approximate weak solution. The proof and further discussion of solutions of the KdV equation with defects (both stable and unstable) can be found in Appendix A. Importantly, we conclude that, for the duration of our long simulations, such natural periodicity defects do not lead to the focusing of energy in the absence of rotation.

Next, we use the mean-free part of these (approximate and exact) weak solutions of the KdV equation as the initial conditions for the Ostrovsky equation (3.31). The effect of rotation on the cnoidal wave with a contraction and expansion defects is shown in the subsequent rows of the same Figure 9, in the left and right columns, respectively, for the interfacial

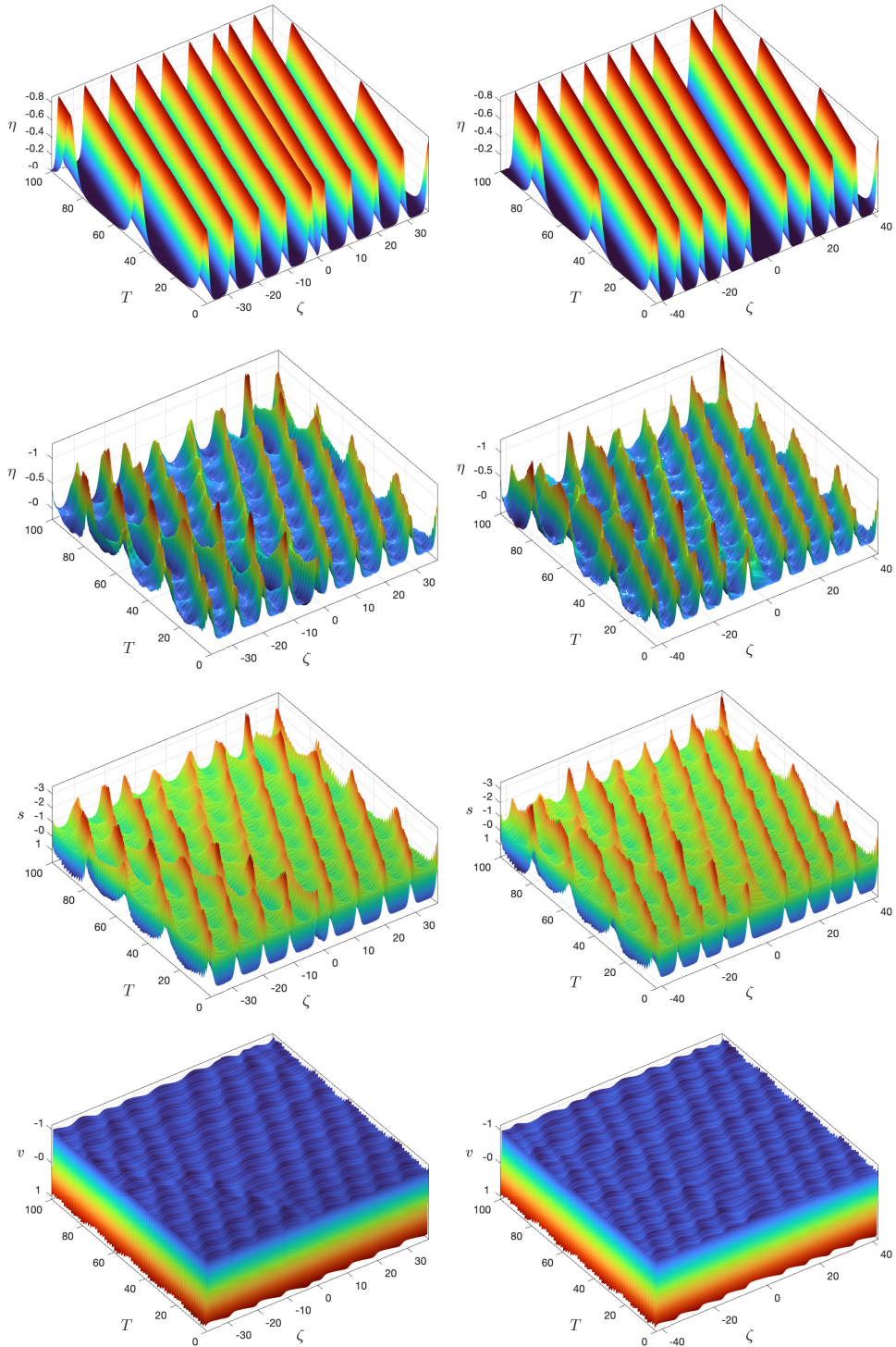


Figure 9: Numerical solution for a cnoidal wave with a contraction (left) and expansion (right) defect initial condition (view from below). First row: interfacial displacement in the absence of rotation. Second row: interfacial displacement under the effect of rotation. Third / fourth row: shear in the direction of wave propagation / orthogonal direction, under the effect of rotation.

Evolution of internal cnoidal waves with local defects in a two-layer fluid with rotation¹⁹

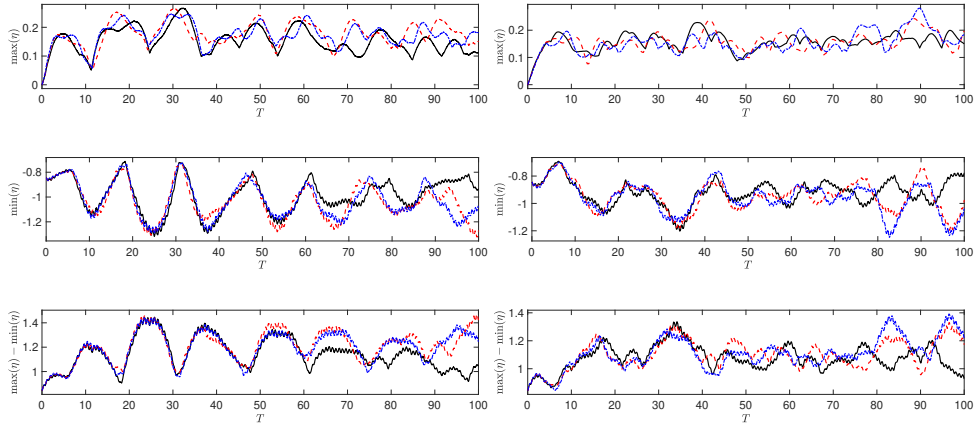


Figure 10: The effect of rotation on the evolution of the maximum, minimum and amplitude of the interfacial displacement for a cnoidal wave with a contraction (left) and expansion (right) defect initial condition. Black solid, red dashed and blue dot-dashed lines correspond to 5, 7 and 9 peaks in the domain, respectively.

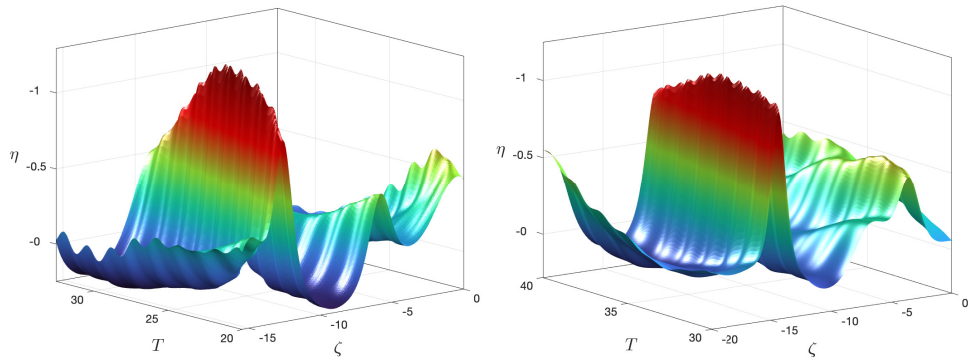


Figure 11: Close-up view from below of the large burst in the interfacial displacement for a cnoidal wave with a contraction (left) and expansion (right) defect around $T = 27$ (left) and $T = 35$ (right), respectively.

displacement (first row), shear in the direction of wave propagation (third row) and shear in the orthogonal direction (fourth row). Here, we see the formation of a strong burst of the interfacial waves and shear in the direction of wave propagation. In the moving reference frame the burst propagates to the left. Qualitatively, this is similar to the behaviour observed in the previous section, where numerical runs were initiated using the breather on a cnoidal wave initial conditions, but the important difference is that this effect is solely due to rotation and no bursts of any kind are present in the absence of rotation.

Figure 10 shows the time evolution of the maximum, minimum and amplitude of the interfacial displacement for both cases of a contraction (left) and expansion (right) periodicity defects. We show that the observed effects of rotation are structurally stable with regard to the size of the computational domain. We experimented with 5, 7 and 9 major peaks in the domain. In the contraction defect case, the computational domains are $2L = 37.42$ (5 peaks), $2L = 55.02$ (7 peaks), $2L = 72.86$ (9 peaks). In the expansion defect case, the computational domains are $2L = 45.44$ (5 peaks), $2L = 63.04$ (7 peaks), $2L = 80.64$ (9 peaks). The remaining numerical parameters are the same as before. The burst forms soon after the initiation of the numerical runs, and the wave continues to grow for a long time after that.

The close-up view of the large wave visible in the free surface elevation is shown in Figure 11 for the time around $T = 25$ (contraction defect, left), with approximately 53% increase in the amplitude compared to the initial condition and around $T = 35$ (expansion defect, right), with an approximately 34% increase in the amplitude compared to the initial condition. Hence, we conclude that under the effect of rotation both contraction and expansion defects present in the otherwise regular cnoidal wave can lead to the emergence of strong bursts of interfacial waves and shear currents in the direction of propagation of the cnoidal wave.

4.4. The effect of rotation on cnoidal waves with generic localised defects

Finally in this section, motivated by the recent numerical and experimental generation of breathers in a fluid conduit during the interaction of a cnoidal wave with a soliton by Maiden and Hoefer (2016); Mao et al. (2023) and generalising this scenario, we initiate numerical runs for our problem with the initial condition which can be described as a cnoidal wave with a generic localised perturbation. Namely, the initial condition is given by the mass-free part of the function

$$\tilde{\eta}^{(0)} = \frac{6\beta_1}{\alpha_1} \left\{ u_2 + (u_3 - u_2) \operatorname{cn}^2 \left[(\zeta - v_c T) \sqrt{\frac{u_3 - u_1}{2}}; m \right] \right\}_{T=0} + A_1 \operatorname{sech}^2 \left[A_2 (\zeta + \zeta_0) \right], \quad (4.12)$$

and $u_1 < u_2 < u_3$ are real, $v_c = 2\beta_1(u_1 + u_2 + u_3)$, $m = (u_3 - u_2)/(u_3 - u_1)$, where A_1 , A_2 and ζ_0 are arbitrary constants.

We experiment with both sets of physical parameters discussed at the beginning of Section 4. For the first set, numerical solutions initiated with the initial condition with a generic localised defect are shown in Figure 12. The computational domain is $2L = 79.20$, with the number of modes $M = 790$, the spatial step $\Delta x \approx 10^{-1}$, the total simulation time $T_{max} = 100$, and the temporal step $\Delta T = 10^{-2}$. The parameters used in the initial condition are $u_1 = -10^{-3}$, $u_2 = 0$, $u_3 = 3$, $A_1 = -0.80$, $A_2 = 1.00$, and $\zeta_0 = -1.30$.

The initial condition introduces a localised perturbation to the otherwise regular cnoidal wave. In our runs, in the absence of rotation, the introduction of such a localised defect leads to the formation of a pair of bright and dark breathers, as well as the clearly noticeable expansion defect, which is shown in the first row of the Figure 12, showing both the view from above (left) and the view from below (right). Qualitatively, this is similar to the waves generated in the interaction of a cnoidal wave with a solitary wave in a conduit in Mao et al. (2023). In the moving reference frame, the bright breather propagates to the right, while the dark breather propagates to the left, and the expansion defect moves with the speed of the cnoidal wave. The effect of rotation on the evolution of the same initial condition is shown in the subsequent rows of the same figure, for the top (left) and bottom (right) views of the interfacial displacement (second row), shear in the direction of wave propagation (third row) and shear in the orthogonal direction (fourth row). There are strong bursts both in the interfacial displacement and shear in the direction of wave propagation, which can be associated with the previously considered types of ‘‘defects’’ in the otherwise regular cnoidal wave. The signal in the shear in the orthogonal direction is again weak. Hence, we conclude that the mechanism of formation of the bursts of strong interfacial displacements and shear in the direction of wave propagation in these simulations can be interpreted as formation of KdV-type breathers and the expansion defect on a cnoidal wave background, with the subsequent effect of rotation.

In order to test our theoretical framework further, we also modelled the effect of rotation on internal waves of elevation, using our second set of parameters discussed at the beginning of Section 4. In Figure 13, the computational domain is $2L = 79.20$, with the number

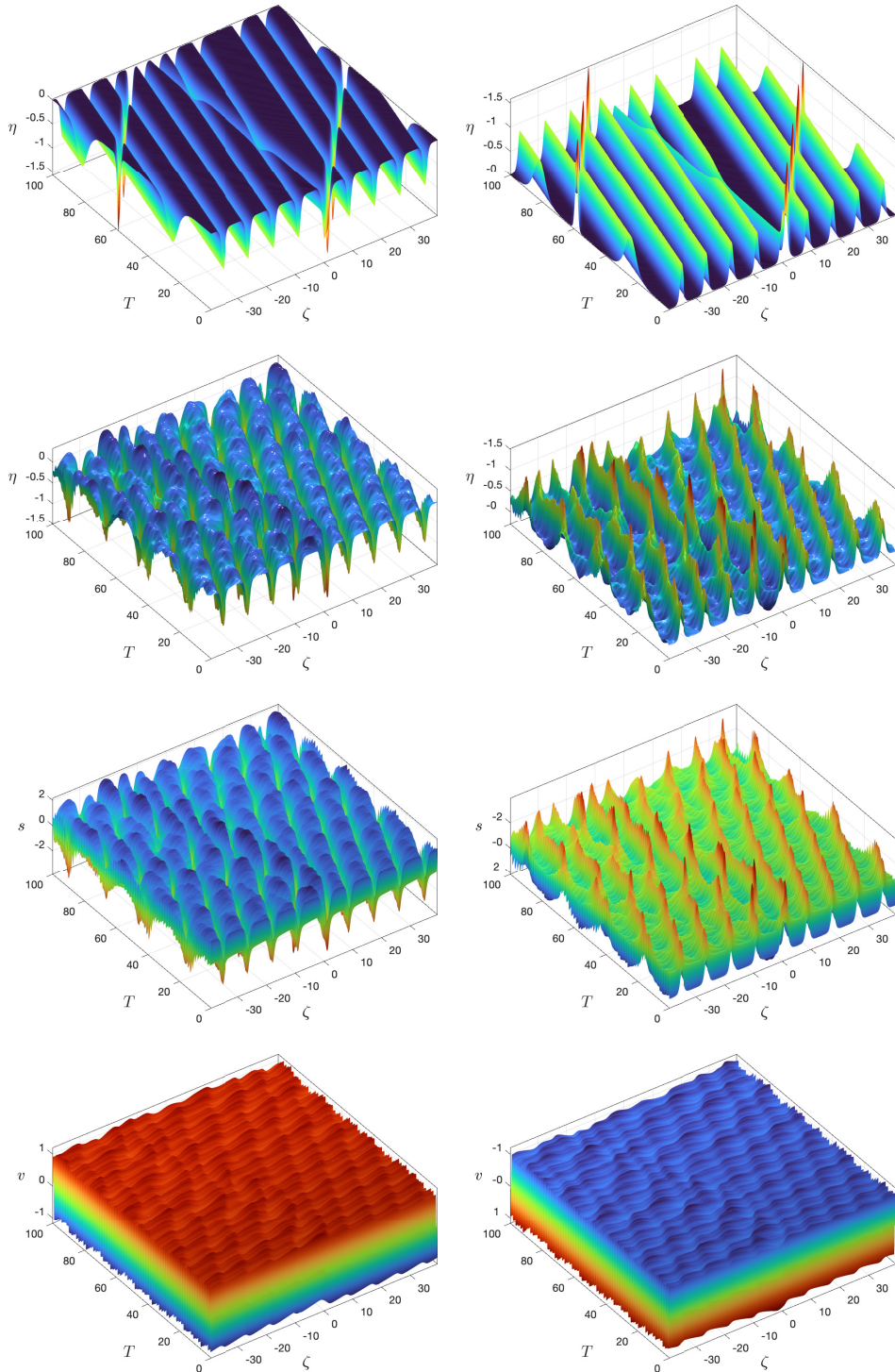


Figure 12: Numerical solution for a cnoidal wave with a generic localised defect initial condition (waves of depression). First row: view from above (left) and below (right) of the interfacial displacement in the absence of rotation. Second row: view from above (left) and below (right) of the interfacial displacement under the effect of rotation. Third / fourth row: view from above (left) and below (right) of the shear in the direction of wave propagation / orthogonal direction, under the effect of rotation.

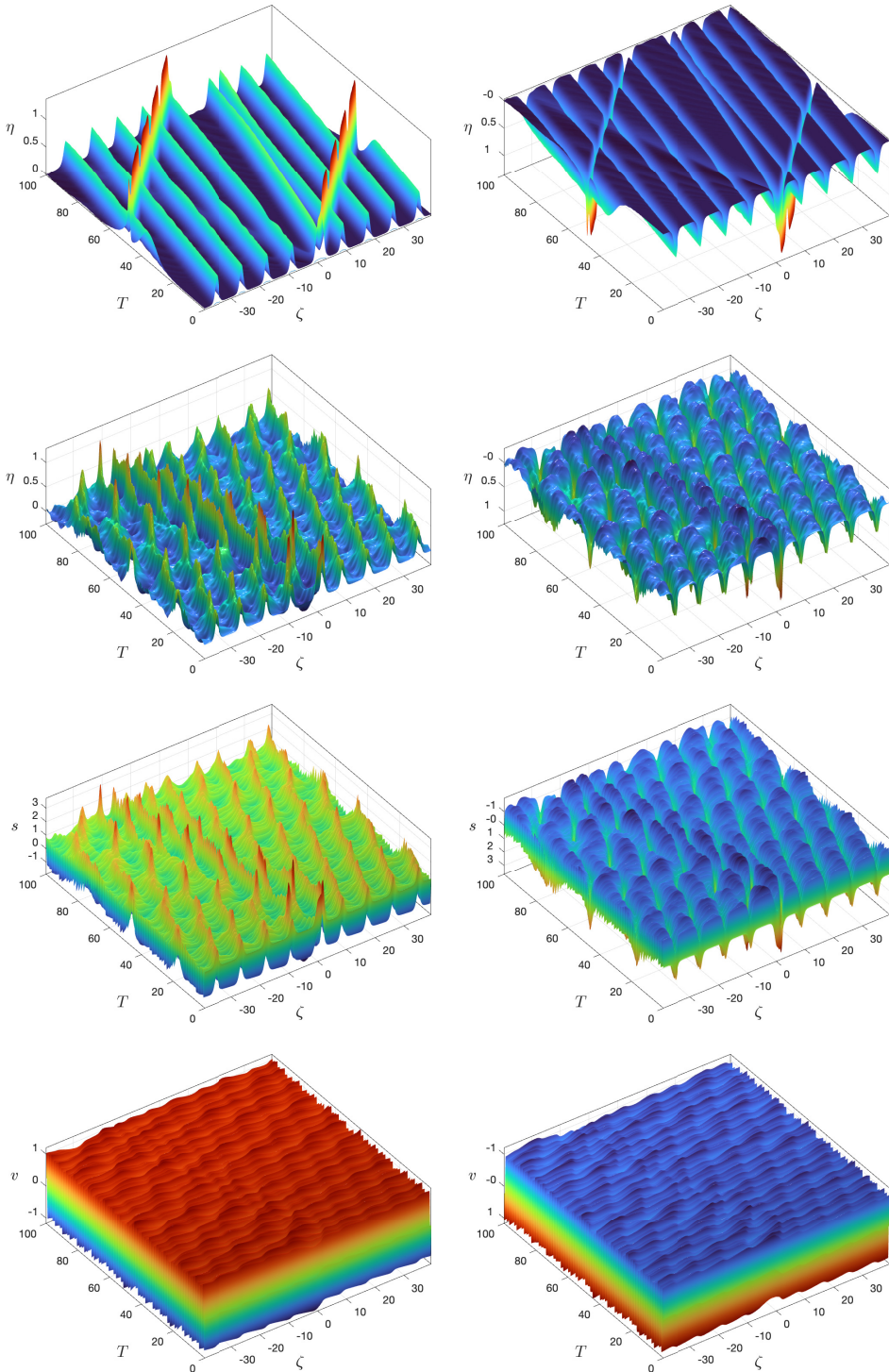


Figure 13: Numerical solution for a cnoidal wave with a generic localised defect initial condition (waves of elevation). First row: view from above (left) and below (right) of the interfacial displacement in the absence of rotation. Second row: view from above (left) and below (right) of the interfacial displacement under the effect of rotation. Third / fourth row: view from above (left) and below (right) of the shear in the direction of wave propagation / orthogonal direction, under the effect of rotation.

Evolution of internal cnoidal waves with local defects in a two-layer fluid with rotation²³

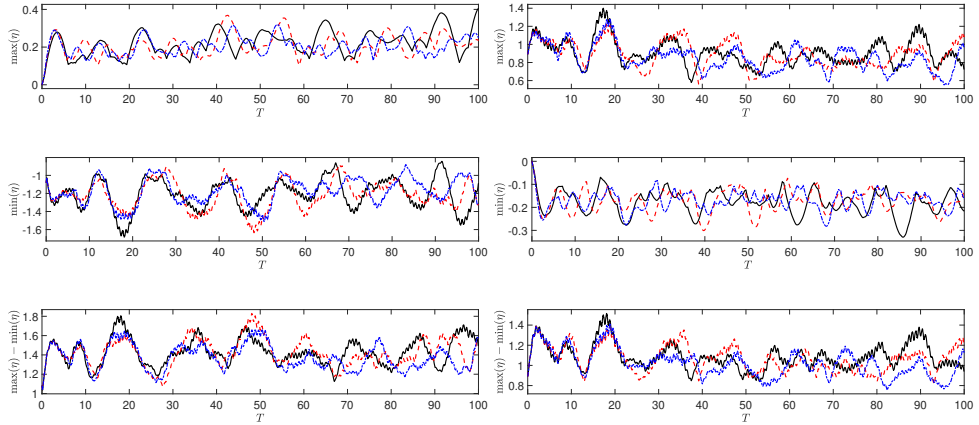


Figure 14: The effect of rotation on the evolution of the maximum, minimum and amplitude of the interfacial displacement for a cnoidal wave with a generic localised defect initial condition: waves of depression (left) and waves of elevation (right). Black solid, red dashed and blue dot-dashed lines correspond to 5, 7 and 9 peaks in the domain, respectively.

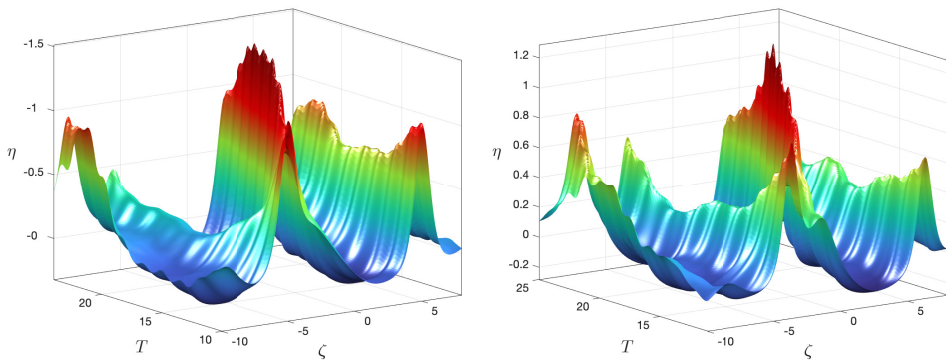


Figure 15: Close-up view from below (left) and above (right) of the large bursts in the interfacial displacement for a cnoidal wave with a generic localised defect initial condition around $T = 19$ for the waves of depression (left) and waves of elevation (right).

of modes $M = 790$, the spatial step $\Delta x \approx 10^{-1}$, the total simulation time $T_{max} = 100$, and the temporal step $\Delta T = 10^{-2}$. The parameters used in the initial condition are $u_1 = -10^{-3}$, $u_2 = 0$, $u_3 = 3$, $A_1 = 0.80$, $A_2 = 1.00$, and $\zeta_0 = -1.30$. Here, the pycnocline is closer to the bottom, the upper layer depth takes 80% of the total depth, whereas in previous cases it was 25%. The results are similar to our previous simulations for internal waves of depression, but here we see the formation of a pair of bright and dark breathers, as before, but also the noticeable formation of both expansion and contraction defects. The comparison of the evolution of maxima, minima and amplitude of the waves shown in Figures 12 and 13 is given in Figure 14, illustrating the growth of the amplitude of the waves and further supporting our interpretation of the observed (in all cases) formation of bursts of strong interfacial displacements and shear in the direction of wave propagation. For both sets, the computational domains are $2L = 44.00$ (5 peaks), $2L = 61.60$ (7 peaks), and $2L = 79.20$ (9 peaks). The remaining numerical parameters are the same as before. The results are structurally stable. The large waves formed at the early stage of our computations are shown

in Figure 15. At around $T = 19$, the first and second sets have approximately 37% and 44% increase, respectively, in the amplitudes relative to the initial conditions.

5. Discussion

In this paper, we addressed several issues related to the modelling of internal waves in the Ostrovsky regime, i.e. in the KdV regime with the account of rotation. We chose Helfrich's f-plane extension (MCC-f) of the two-layer MCC model as our parent system (it would be better to call the system MMCC model, recognising the contribution of Maltseva 1989). The MCC-f model has similar properties to the full Euler equations with rotation with respect to construction of the weakly-nonlinear solution, but the technical details related to the derivation are more manageable. In our derivation, we represented all field variables as the sums of time-dependent mean values and both spatially- and time-dependent deviations from these evolving means. We considered periodic solutions, and mean-field equations were obtained by averaging the equations over the period of the problem. In contrast to our previous research within the scope of the Boussinesq-type equations, the resulting equations for the mean fields turned out to be coupled to the equations for the deviations, which presented a significant new challenge. We managed to construct a large class of solutions for unidirectional waves by introducing two slow-time variables, and simultaneously constructing asymptotic expansions in powers of the square root of the amplitude parameter (as opposed to the traditional derivation of the Ostrovsky equation with just one slow time and in powers of the amplitude parameter). Since the resulting reduced model, the Ostrovsky equation, has been derived for the zero-mean deviations by construction, the so-called "zero-mean contradiction" meaning the existence of the zero-mean constraints on all field variables of the parent system has been by-passed.

Next, we used the constructed weakly-nonlinear solution combined with extensive numerical modelling using the Ostrovsky equation in order to study the effect of rotation on the evolution of internal waves with initial conditions in the form of the KdV cnoidal waves, but with various local defects. We built the phenomenological framework by considering pure bright and dark breather on a cnoidal wave initial conditions and cnoidal waves with contraction and expansion periodicity defects. The latter defects were introduced 'by hand', by modifying the cnoidal wave solution near the trough in between the two peaks, and we showed that such functions satisfy all (infinitely many) conservation laws of the KdV equation. Moreover, the cnoidal waves with an expansion defect also have continuous first derivative, satisfying the so-called 'corner condition' necessary for it to be a non-smooth extremal of the relevant variational problem (see Appendix A). It must be noted that in our numerical runs both the contraction and expansion defects were long-lived, and a cnoidal wave with an expansion defect behaved very close to an exact travelling wave of the KdV equation. The important difference between the defects represented by dislocation- (bright and dark breather) and periodicity- (contraction and expansion) perturbations of the cnoidal wave is that the second type does not lead to formation of bursts in the absence of rotation. Qualitatively, both types of defects lead to formation of bursts of large interfacial displacements and shear in the direction of wave propagation, under the effect of rotation.

Finally, we considered initial conditions in the form of cnoidal waves with generic localised defects. Our modelling has shown that, in the absence of rotation, such initial conditions typically produce a pair of a fast-moving bright and slow-moving dark breathers and expansion and contraction periodicity defects, moving with the speed of the cnoidal wave. Under the effect of rotation, the splitting of a generic localised defect into these 'basic' defects is followed by formation of several bursts of interfacial displacements and shear in the direction of wave propagation, which can be associated with the effect of rotation

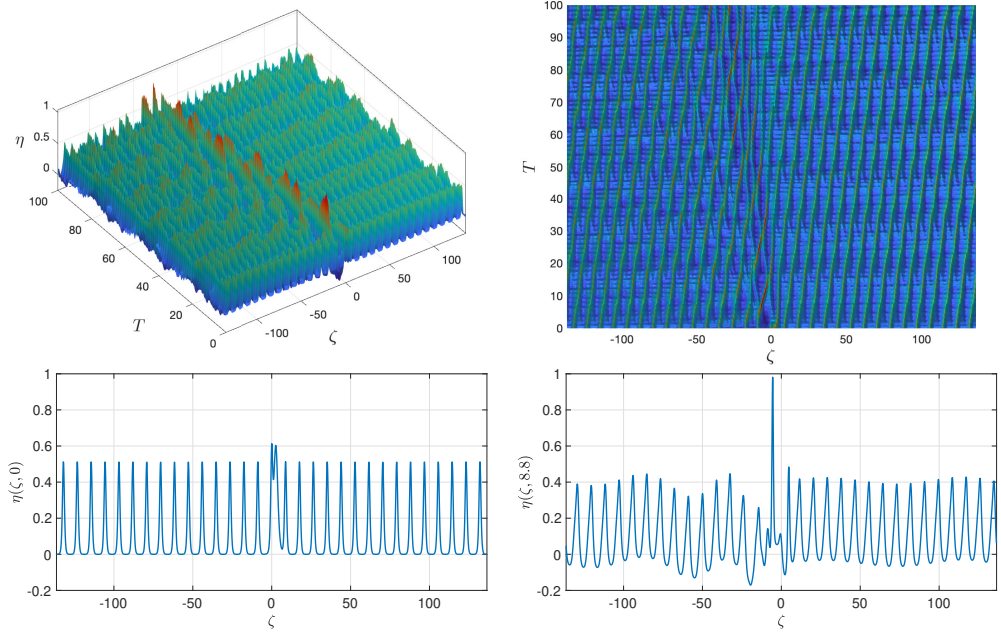


Figure 16: Rogue wave generation: 3D and 2D views of the interfacial displacement from above (top row) and initial condition at $T = 0$ vs interfacial displacement at $T = 8.8$ (bottom row).

on breathers and the periodicity defects. In all simulations the large bursts propagated to the left in our moving reference frame, i.e. slower than the linear long-wave speed. In this study we did not aim to systematically investigate the probability of generation of rogue waves due to this scenario (in the sense of the classical definition of rogue waves as the waves with the amplitude being more than twice the significant wave height), but it is worth mentioning that it did not take much effort to generate the rogue wave shown in Figure 16 using the same physical parameters as in Figure (13) and initial condition (4.12) with $u_1 = -10^{-3}$, $u_2 = 0$, $u_3 = 3$, $A_1 = 0.60$, $A_2 = 0.60$, and $\zeta_0 = -2.60$. The computational domain is $2L = 272.81$ with the number of modes $M = 2726$, the spatial step $\Delta x \approx 10^{-1}$, the total simulation time $T_{max} = 100$, with the temporal step $\Delta T = 10^{-2}$. This could be an interesting direction of further research.

We hope that our study sheds light both on the typical structure of nearly cnoidal waves (with defects) observed in oceanic observations (see, for example, Figure 1 in the Introduction), and on the role of rotation in the formation of bursts of large interfacial displacements and shear in the direction of wave propagation. Further developments could concern bi-directional propagation and effects related to barotropic transport, which were discussed in the construction of the weakly-nonlinear solution, but were left out of scope of the subsequent modelling. Another issue which was left out of scope of the present study was the effect of the depth-dependent shear currents (see Hooper et al. (2021); Tseluiko et al. (2023) for the recent developments related to the presence of a long-wave instability, in the absence of rotation). As a by-product of our study we constructed some curious weak solutions of the KdV equation, whose smoothed counterparts naturally emerged in the evolution of initial conditions in the form of cnoidal waves with local defects. It would be interesting to investigate whether similar solutions can be found in other integrable models, and what is their meaning and role in the relevant physical contexts.

6. Acknowledgements

Karima Khusnutdinova is grateful to Evgeny Ferapontov, Sergey Gavrilyuk, Boris Kruglikov and Victor Shrira for useful discussions, and to Zakhar Makridin and Nikolay Makarenko for sending the paper Maltseva (1989). Korsarun Nirunwiroj would like to acknowledge the Royal Thai Government Scholarship supporting his postgraduate studies at Loughborough University. Karima Khusnutdinova would like to thank the Isaac Newton Institute for Mathematical Sciences, Cambridge, for support and hospitality during the programme “Emergent phenomena in nonlinear dispersive waves”, where partial work on this paper was undertaken. This work was supported by EPSRC grant EP/R014604/1.

Appendix A.

The KdV equation

$$u_t - 6uu_x + u_{xxx} = 0$$

can be represented in the form of a conservation law

$$\frac{\partial u}{\partial t} + \frac{\partial}{\partial x} \left(-3u^2 + u_{xx} \right) = 0. \quad (\text{A } 1)$$

Equation (A 1) implies conservation of ‘mass’,

$$\frac{d}{dt} \int_{-L}^L u dx = 0, \quad (\text{A } 2)$$

provided the function $u(x, t)$ either vanishes together with its spatial derivatives as $L \rightarrow \infty$, or it is spatially periodic on the interval $[-L, L]$. The latter case is considered in our paper.

Using simple algebra, one can also obtain conservation laws for ‘momentum’

$$\frac{\partial}{\partial t} \frac{u^2}{2} + \frac{\partial}{\partial x} \left(uu_{xx} - \frac{1}{2}u_x^2 - 2u^3 \right) = 0 \quad (\text{A } 3)$$

and ‘energy’

$$\frac{\partial}{\partial t} \left(u^3 + \frac{1}{2}u_x^2 \right) + \frac{\partial}{\partial x} \left(-\frac{9}{2}u^4 + 3u^2u_{xx} - 6uu_x^2 + u_xu_{xxx} - \frac{1}{2}u_{xx}^2 \right) = 0. \quad (\text{A } 4)$$

It is well known that the KdV equation has infinitely many polynomial conservation laws, which can be proven using a generating function (Miura et al. 1968). Indeed, the Gardner transformation

$$u = w + \epsilon w_x + \epsilon^2 w^2, \quad (\text{A } 5)$$

where ϵ is the grading parameter, yields

$$u_t - 6uu_x + u_{xxx} = (1 + 2\epsilon^2 w + \epsilon \partial_x) [w_t + (w_{xx} - 3w^2 - 2\epsilon^2 w^3)_x] = 0. \quad (\text{A } 6)$$

Therefore, if $w(x, t)$ satisfies the conservation law

$$w_t + (w_{xx} - 3w^2 - 2\epsilon^2 w^3)_x = 0, \quad (\text{A } 7)$$

then $u(x, t)$ satisfies the KdV equation. Next, one represents w in the form of an asymptotic expansion in powers of ϵ :

$$w = \sum_{n=0}^{\infty} \epsilon^n w_n. \quad (\text{A } 8)$$

Collecting the coefficients of equal powers of ϵ in (A 5) gives us

$$w_0 = u, \quad w_1 = -w_{0x} = -u_x, \quad w_2 = -w_{1x} - w_0^2 = u_{xx} - u^2, \quad (\text{A } 9)$$

$$w_n = -w_{n-1,x} - \sum_{k=0}^{n-2} w_k w_{n-2-k} \quad \text{for } n \geq 2. \quad (\text{A } 10)$$

Now, substituting expansion (A 8) into (A 7) one obtains an infinite series of the KdV conservation laws as the coefficients at even powers of ϵ . The coefficients of odd powers are exact differentials (referred to as ‘trivial conservation laws’, see Miura et al. 1968, for the details).

The integrals

$$I_n = \int_{-L}^L w_{2n} dx, \quad n = 0, 1, 2, \dots$$

are called ‘Kruskal integrals’. In particular, the first three integrals take the form

$$I_1 = \int_{-L}^L u dx, \quad I_2 = \int_{-L}^L \frac{1}{2} u^2 dx, \quad I_3 = \int_{-L}^L \left(u^3 + \frac{1}{2} u_x^2 \right) dx.$$

Next, to prove that cnoidal waves with our contraction and expansion defects satisfy all conservation laws of the KdV equation, we also need a recurrence formula for the fluxes. Substituting expansion (A 8) into (A 7) we obtain

$$w_{xxx} - 3w^2 + 2\epsilon^2 w^3 = \sum_{n=0}^{\infty} \epsilon^n f_n, \quad (\text{A } 11)$$

where

$$f_0 = w_{0,xx} - 2w_0^2, \quad f_1 = w_{1,xx} - 6w_0 w_1, \quad f_2 = w_{2,xx} - 3w_1^2 - 6w_1 w_2 + 2w_0^3, \quad (\text{A } 12)$$

$$f_n = w_{n,xx} - 3 \sum_{k=0}^n w_k w_{n-k} + 2 \sum_{k+l+m=n-2} w_k w_l w_m \quad \text{for } n \geq 2, \quad (\text{A } 13)$$

with the last summation being over all triples of integers (k, l, m) such that $k + l + m = n - 2$.

Let us now consider a cnoidal wave with a contraction defect, as shown in the first row of Figure 17. This wave is constructed by extracting a symmetric interval around a trough between two neighbouring peaks and gluing the remaining parts together. Let us denote the period of the cnoidal wave by ℓ . If we consider m peaks in the domain, then without the defect $L = m\ell/2$. With the defect, given that the length of the extracted symmetric interval is d , then $L = (m\ell - d)/2$. The resulting function has a corner at one point in the periodic domain $[-L, L]$, and the graph is symmetric about the vertical axis passing through that point. Let us denote this point by x_0 . We can then associate the origin of the moving reference frame with x_0 , i.e. assume $x_0 = 0$, and the function $w_0 = u$ will be even in that frame. From the recurrence relation (A 10), we observe that functions w_{2n} are even and w_{2n+1} are odd. Recalling that non-trivial conservation laws correspond to even values $2n$, we deduce from the recurrence relation (A 13) that the corresponding fluxes f_{2n} can only contain terms representing even functions. Therefore,

$$\frac{d}{dt} I_n = - \int_{-L}^0 f_{2n,x} dx - \int_0^L f_{2n,x} dx \quad (\text{A } 14)$$

$$= - [f_{2n}]_{-L}^0 - [f_{2n}]_0^L = 0 \quad (\text{A } 15)$$

by periodicity and since the flux f_{2n} is an even function.

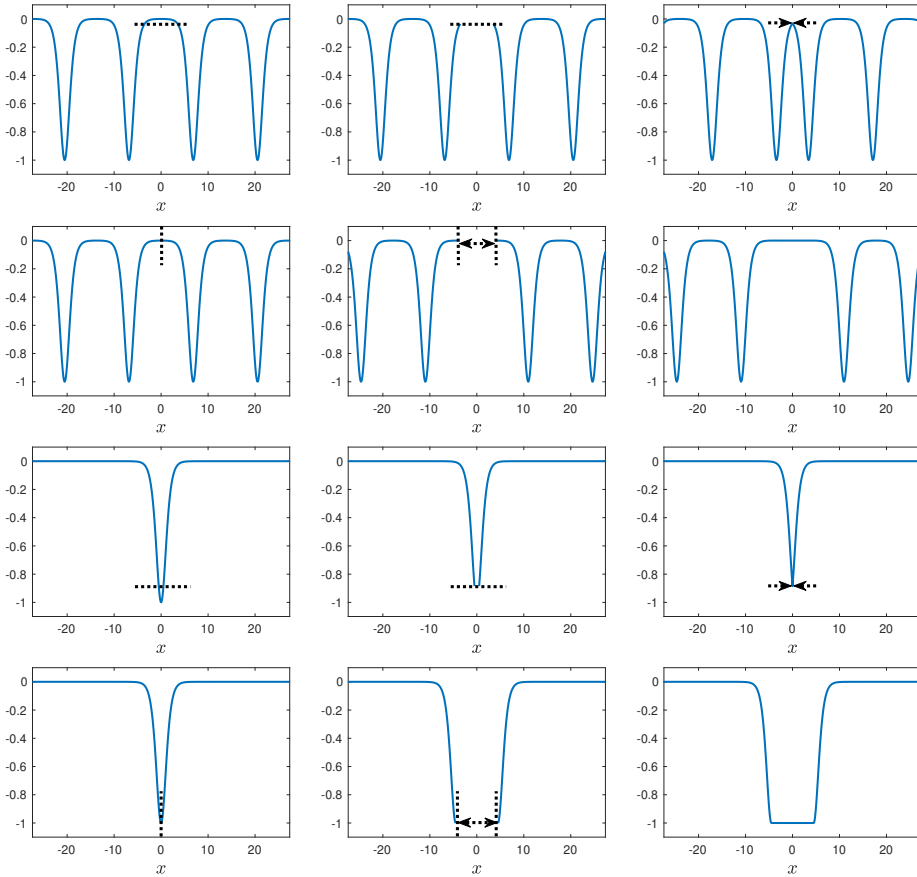


Figure 17: Schematic of construction of long-lived approximate and exact weak solutions of the KdV equation in the form of a cnoidal wave with a contraction and expansion periodicity defects (first and second rows, respectively), and a short-lived soliton with similar amplitude defects (third and fourth rows, respectively).

Similarly, we can consider a cnoidal wave with an expansion defect, as shown in the second row of Figure 17. This wave is constructed by cutting at a trough of the cnoidal wave between two peaks and symmetrically adding a segment of straight line at the corresponding level. (This can be generalised similarly to the contraction defect by first extracting a small part close to the trough, symmetrically inserting a segment of straight line and gluing the remaining parts to it. The resulting functions will also satisfy all conservation laws of the KdV equation.) Let the x -coordinates of the left and right endpoints of the line segment be denoted by x_1 and x_2 , respectively. We can choose our reference frame to have $x_1 = -x_2 = -x_d$. Consequently,

$$\frac{d}{dt}I_n = - \int_{-L}^{-x_d} f_{2n_x} dx - \int_{-x_d}^{x_d} f_{2n_x} dx - \int_{x_d}^L f_{2n_x} dx \quad (\text{A } 16)$$

$$= - [f_{2n}]_{-L}^{-x_d} - [f_{2n}]_{-x_d}^{x_d} - [f_{2n}]_{x_d}^L = 0 \quad (\text{A } 17)$$

by periodicity, the constant value of f_{2n} on the interval $[-x_d, x_d]$, and since the flux f_{2n} is an even function.

Another way to proving the above relies on using that all non-trivial fluxes f_{2n} are polynomial functions of even weight with respect to the scaling symmetries of the KdV

equation. This also implies that the fluxes f_{2n} are even functions, and the rest follows from that.

Next, the KdV equation (4.1) can be written in Lagrangian form

$$\delta \int \mathcal{L} dx dt = 0, \quad \text{where} \quad \mathcal{L} = \frac{1}{2} \phi_t \phi_x - \phi_x^3 - \frac{1}{2} \phi_{xx}^2, \quad u = \phi_x. \quad (\text{A } 18)$$

The weak solutions considered here are non-smooth travelling waves. Hence, the Lagrangian density (A 18) becomes a function of u and u_x : $\mathcal{L} = \mathcal{L}(u, u_x)$. The Weirstrass-Erdmann corner conditions for broken extremals require the continuity of

$$\frac{\partial \mathcal{L}}{\partial u_x} \quad \text{and} \quad \mathcal{L} - u_x \frac{\partial \mathcal{L}}{\partial u_x} \quad (\text{A } 19)$$

at each junction (e.g. Fox 1954), which leads to the requirement of continuity of u_x , since u is continuous (see also Gavrilyuk and Shyue 2022 for a relevant discussion in the context of the Benjamin-Bona-Mahoney equation). This condition is satisfied exactly for a cnoidal wave with an expansion defect, and approximately for a cnoidal wave with a contraction defect, provided we cut close to extremum. The smoothed counterparts of cnoidal waves with both expansion and contraction defects were long-lived in our numerical simulations, with the former function behaving very close to a travelling wave solution. Therefore, it makes sense to view the corresponding functions as the exact and approximate weak travelling wave solutions of the KdV equation, respectively.

Having observed that the constructed weak solutions are long-lived (with the expansion defects possibly even stable), it is also tempting to try to construct similar solutions by cutting around the peak rather than trough. In contrast to the previous cases, this can be done for a single peak as well, starting from the exact soliton solution, as shown in the third and fourth rows of Figure 17. However, in numerical runs, the smoothed counterparts of these solutions turned out to be unstable and short-lived, fissioning and giving rise to the usual solitons, in full agreement with the Inverse Scattering Transform (IST) predictions (Gardner et al. 1967, see also Drazin and Johnson 1989) for the respective smoothed initial conditions.

Appendix B.

The Ostrovsky equation

$$(u_T + \alpha_1 u u_\zeta + \beta_1 u_\zeta \zeta_\zeta)_\zeta = \gamma_1 u \quad (\text{B } 1)$$

is numerically solved by pseudospectral methods (see Fornberg 1996; Trefethen 2000), which usually offer the highest accuracy and computational efficiency for smooth data on periodic domains. By implementing the Fast Fourier Transform (FFT) algorithm for spatial derivatives and the fourth-order Runge–Kutta scheme for time stepping, the method yields accurate approximation of the solution to the differential equation.

The spatial domain is discretised by M equidistant points with spacing $\Delta x = 2\pi/M$. Then, the discrete Fourier transform of the equation with respect to ζ gives

$$\hat{u}_T - i(k^3 \beta_1 - \frac{\gamma_1}{k}) \hat{u} = -\frac{i k \alpha_1}{2} (\hat{u}^2),$$

where k is the scaled wavenumber. We use the 4th-order Runge–Kutta scheme for temporal integration. By the integrating factor method of Kassam and Trefethen (e.g. Trefethen 2000), we multiply the equation by $K = \exp[-i(k^3 \beta_1 - \frac{\gamma_1}{k})T]$ to obtain

$$\hat{U}_T = -\frac{i k \alpha_1}{2} K \mathcal{F} \{ (\mathcal{F}^{-1} \left[\frac{\hat{U}}{K} \right])^2 \},$$

where $\hat{U} = \exp[-i(k^3\beta_1 - \frac{\gamma_1}{k})T] \hat{u} = K\hat{u}$ and \mathcal{F} is the Fourier transform. Discretising the time domain as $T_n = n\Delta T$, and introducing the function

$$E = \exp[\frac{i}{2}(k^3\beta_1 - \frac{\gamma_1}{k})\Delta T],$$

the optimised Runge–Kutta time stepping has the form

$$\hat{u}^{(n+1)} = E^2\hat{u}^{(n)} + \frac{1}{6}[E^2k_1 + 2E(k_2 + k_3) + k_4],$$

where

$$k_1 = -\frac{ik\alpha_1}{2}\Delta T \mathcal{F}\{(\mathcal{F}^{-1}[\hat{u}^{(n)}])^2\},$$

$$k_2 = -\frac{ik\alpha_1}{2}\Delta T \mathcal{F}\{(\mathcal{F}^{-1}[E(\hat{u}^{(n)} + k_1/2)])^2\},$$

$$k_3 = -\frac{ik\alpha_1}{2}\Delta T \mathcal{F}\{(\mathcal{F}^{-1}[E\hat{u}^{(n)} + k_2/2])^2\},$$

$$k_4 = -\frac{ik\alpha_1}{2}\Delta T \mathcal{F}\{(\mathcal{F}^{-1}[E^2\hat{u}^{(n)} + Ek_3])^2\}.$$

REFERENCES

- AGAFONTSEV, D., GELASH, A., RANDOUX, S., SURET, P. 2024 Multisoliton interactions approximating the dynamics of breather solutions. *Stud. Appl. Math.*, **152**, 810-834.
- ALIAS, A., GRIMSHAW, R. H. J., KHUSNUTDINOVA, K. R. 2013 On strongly interacting internal waves in a rotating ocean and coupled Ostrovsky equations. *Chaos*, **23**, 023121.
- ALIAS, A., GRIMSHAW, R. H. J., KHUSNUTDINOVA, K.R. 2014 Coupled Ostrovsky equations for internal waves in a shear flow. *Phys. Fluids*, **26**, 126603.
- BENILOV, E. S. 1992 On the surface waves in a shallow channel with an uneven bottom. *Stud. Appl. Math.*, **87**, 1-14.
- BERTOLA, M., JENKINS, R., TOVBIS, A. 2023 Partial degeneration of finite gap solutions to the Korteweg-de Vries equation: soliton gas and scattering on elliptic backgrounds. *Nonlinearity*, **36**, 3622.
- BOKAEYAN, M., ANKIEWICZ, A., AKHMEDIEV, N. 2019 Bright and dark rogue internal waves: The Gardner equation approach. *Phys. Rev. E*, **99**, 062224.
- BONA, J. L., LANNES, D., SAUT, J. C. 2008 Asymptotic models for internal waves. *J. Math. Pure Appl.*, **89**, 538-566.
- BOUSSINESQ, J. 1871 Theorie de l'intumescence liquid appelee onde solitaire ou de traslation, se propageant dans un canal rectangulaire, *Comptes Rendus Acad. Sci. (Paris)*, **72**, 755 - 759.
- CHABCHOUB, A., HOFFMAN, N., ONORATO, M., GENTY, G., DUDLEY, J.M., AKHMEDIEV, N. 2013 Hydrodynamic supercontinuum. *Phys. Rev. Lett.*, **111**, 054104.
- CHABCHOUB, A., SLUNYAEV, A., HOFFMAN, N., GENTY, G., DIAS F., KIBLER, B., DUDLEY, J.M., AKHMEDIEV, N. 2021 The Peregrine breather on the zero-background limit as the two-soliton degenerate solution: an experimental study. *Front. Phys.*, **9**, 633549.
- CHANDRAMOULI, S., MAO, Y., HOEFER, M.A. 2024 Bright traveling breathers in media with long-range, nonconvex dispersion. *Phys. Rev. E*, **109**, 034212.
- CHOI, J., BOKHOVE, O., KALOGIROU, A., KELMANSO, M.A. 2022 Numerical experiments on extreme waves through oblique–soliton Interactions. *Water Waves*, **4**, 139-179.
- CHOI, W., CAMASSA, R. 1998 Weakly nonlinear internal waves in a two-fluid system. *J. Fluid Mech.*, **313**, 83-103.
- CHOI, W., CAMASSA, R. 1999 Fully nonlinear internal waves in a two-fluid system. *J. Fluid Mech.*, **396**, 1-36.
- CONGY, T., EL, G., ROBERTI, G., TOVBIS, A., RANDOUX, S., SURET, P. 2024 Statistics of Extreme Events in Integrable Turbulence. *Phys. Rev. Lett.*, **132**, 207201.
- DRAZIN, P. G., JOHNSON, R. S. 1989 Solitons: an Introduction. *Cambridge University Press*.
- FLAMARION, M.V., PELINOVSKY, E., DIDENKULOVA, E. 2024 Non-integrable soliton gas: The Schamel equation framework. *Chaos, Solitons & Fractals*, **180**, 113870.

- FORNBERG, B. 1996 A Practical Guide to Pseudospectral Methods. *Cambridge University Press*.
- FOX, C. 1954 An Introduction to the Calculus of Variations. *Oxford University Press*.
- GARDNER, C. S., GREENE, J. M., KRUSKAL, M. D., MIURA, R. M. 1967 Method for solving the Korteweg-de Vries equation. *Phys. Rev. Lett.*, **19**, 1095-1097.
- GERKEMA, T. 1996 A unified model for the generation and fission of internal tides in a rotating ocean. *J. Mar. Res.*, **54**, 421-450.
- GAVRILYUK, S., NKONGA, B., SHYUE, K.-M., TRUSKINOVSKY, L. 2020 Stationary shock-like transition fronts in dispersive systems. *Nonlinearity*, **33**, 5477-5509.
- GAVRILYUK, S., NKONGA, B., SHYUE, K.-M. 2024 The conduit equation: hyperbolic approximation and generalized Riemann problem. *J. Comp. Phys.*, **2024**, 113232.
- GAVRILYUK, S., SHYUE, K.-M. 2022 Singular solutions of the BBM equation: analytical. and numerical study. *Nonlinearity*, **35**, 388-410.
- GRAVA, T., MCLAUGHLIN, K. D., GIROTTI, M., JENKINS, R., MINAKOV, A. 2023 Soliton versus the gas: Fredholm determinants, analysis, and the rapid oscillations behind the kinetic equation. *Comm. Pure Appl. Math.*, **76**, 3233-3299.
- GRIMSHAW, R., OSTROVSKY, L., SHRIRA, V. I., STEPANYANTS, Y. A. 1998 Long nonlinear surface and internal gravity waves in a rotating ocean. *Surv. Geophys.*, **19**, 289-338.
- GRIMSHAW R., PELINOVSKY E. N., TALIPOVA T. G., KURKINA O. E. 2010 Internal solitary waves: propagation, deformation and disintegration. *Nonlin Proc. Geophys.*, **17**, 633-649.
- GRIMSHAW R. H. J., HELFRICH K. R., JOHNSON E. R. 2013. Experimental study of the effect of rotation on large amplitude internal waves. *Phys Fluids.*, **25**, 056602.
- HE, Y., WITT, A., TRILLO, S., CHABCHOUB, A., HOFFMANN, N. 2022 Extreme wave excitation from localized phase-shift perturbations. *Physical Review E*, **106(4)**, L043101.
- HELFRICH, K. R., MELVILLE, W. K. 2006 Long nonlinear internal waves. *Annu. Rev. Fluid Mech.*, **38**, 395-425.
- HELFRICH, K. R. 2007 Decay and return of internal solitary waves with rotation. *Phys. Fluids*, **19**, 026601.
- HOEFER, M.A., MUCALICA, A., PELINOVSKY, D.E. 2023 KdV breather on a cnoidal wave background. *J. Phys. A: Math. Theor.*, **56**, 185701.
- HOOPER, C., KHUSNUTDINOVA, K. R., GRIMSHAW, R. H. J. 2021 Wavefronts and modal structure of long surface and internal ring waves on a parallel shear current. *J. Fluid Mech.*, **927**, A37.
- JOHNSON, R. S. 1997 A Modern Introduction to the Mathematical Theory of Water Waves. *Cambridge University Press*.
- KAMCHATNOV, A.M. 2000 Nonlinear Periodic Waves and their Modulations. *World Scientific Publishing*.
- KEDZIORA, D.J., ANKIEWICZ, A., AKHMEDIEV, N. 2014 Rogue waves and solitons on a cnoidal background. *Eur. Phys. J. Special Topics*, **223**, 43-62.
- KHARIF, C., PELINOVSKY, E., SLUNYAEV, A. 2009 Rogue Waves in the Ocean. In series: Advances in Geophysical and Environmental Mechanics and Mathematics. *Springer*.
- KHUSNUTDINOVA, K. R., MOORE K. R., PELINOVSKY, D. E. 2014 Validity of the weakly nonlinear solution of the Cauchy problem for the Boussinesq-type equation. *Stud. Appl. Math.*, **133**, 52-83.
- KHUSNUTDINOVA, K.R., ZHANG, X. 2016 Long ring waves in a stratified fluid over a shear flow, *J. Fluid Mech.*, **794**, 17-44.
- KHUSNUTDINOVA, K. R., TRANTER, M. R. 2019 D'Alembert-type solution of the Cauchy problem for the Boussinesq-Klein-Gordon equation *Stud. Appl. Math.*, **142**, 551-585.
- KHUSNUTDINOVA, K. R., TRANTER, M. R. 2022 Periodic solutions of coupled Boussinesq equations and Ostrovsky-type models free from zero-mass contradiction, *Chaos*, **32**, 113132.
- KORTEWEG, D.J., DE VRIES, G. 1895 On the change of form of long waves advancing in a rectangular canal, and on a new type of long stationary waves, *Phil. Mag.*, **39**, 422-443.
- KUZNETSOV, E.A., MIKHAILOV, A.V. 1975 Stability of stationary waves in nonlinear weakly dispersive media, *Sov. Phys. JETP*, **40**, 855-859.
- MAIDEN, M.D., HOEFER, M.A. 2016 Modulations of viscous fluid conduit periodic waves, *Proc. R. Soc. A*, **472**, 20160533.
- Mao, Y., Chandramouli, S., Xu, W., Hoefler, M. 2023 Observation of travelling breathers and their scattering in a two-fluid system, *Phys. Rev. Lett.*, **131**, 147201.
- MALTSEVA, Zh. L. 1989 Unsteady long waves in a two-layer fluid. *Dinamika Sploshn. Sredy*, **93**, pp. 96-110. (in Russian).

- MIURA, R.M., GARDNER, C.S., KRUSKAL, M.D. 1968 Korteweg - de Vries equation and generalisations. II. Existence of conservation laws and constants of motion, *J. Math. Phys.*, **9**, 1204-1209.
- MİYATA, M. 1988 Long internal waves of large amplitude. *Nonlinear water waves*, Springer, Berlin, Heidelberg, pp. 399-406.
- ONORATO, M., RESIDORI, S., BORTOLOZZO, U., MONTINA, A., ARECCHI, F.T. 2013 Rogue waves and their generating mechanisms in different physical contexts. *Phys. Reports*, **528**, 47-89.
- OSTROVSKY, L. A. 1978 Nonlinear internal waves in a rotating ocean. *Oceanology (Engl. Transl.)*, **18**, 119-125.
- OSTROVSKY, L. A., PELINOVSKY, E. N., SHRIRA, V. I., STEPANYANTS, Y. A. 2015 Beyond the KdV: Post-explosion development. *Chaos*, **25**, 097620.
- OSTROVSKY, L. A., PELINOVSKY, E. N., SHRIRA, V. I., STEPANYANTS, Y. A. 2024 Localized wave structures: Solitons and beyond. *Chaos*, **34**, 062101.
- PELINOVSKY, E., SLUNYAEV, A.V. 2016 The role of multiple soliton and breather interactions in generation of rogue waves: the mKdV framework. *Phys. Rev. Lett*, **117**, 214501.
- SLUNYAEV, A. 2024 Soliton groups and extreme wave occurrence in simulated directional sea waves. *Phys. Fluids*, **36**, 077101.
- SLUNYAEV, A.V., SHRIRA, V.I. 2023 Extreme dynamics of wave groups on jet currents. *Phys. Fluids*, **25**, 126606.
- STANTON, T. P., OSTROVSKY, L. A. 1998 Observations of highly nonlinear internal solitons over the continental shelf. *Geoph. Res. Lett.*, **25**, 2695-2698.
- STEPANYANTS, Y. A. 2020 Nonlinear waves in a rotating ocean (The Ostrovsky Equation and Its generalizations and applications). *Izv. Atmos. Ocean. Phys.*, **56**, 16-32.
- TREFETHEN, L.N. 2000 Spectral Methods in MATLAB. *SIAM*.
- TSELUIKO, D., ALHARTHI, N. S., BARROS, R., KHUSNUTDINOVA, K. R. 2023 Internal ring waves in a three-layer fluid on a current with a constant vertical shear. *Nonlinearity*, **36**, 3431-3466.
- WHITFIELD A. J., JOHNSON E. R. 2017 Whitham modulation theory for the Ostrovsky equation. *Proc. R. Soc. A*, **473**, 20160709.
- ZAKHAROV, V.E. 2009 Turbulence in integrable systems. *Stud. Appl. Math.*, **2009**, 219-234.